

Spatiotemporal mode-locking in multimode fiber lasers

Logan G. Wright¹, Demetrios N. Christodoulides², and Frank W. Wise¹

1. School of Applied and Engineering Physics, Cornell University, Ithaca, New York 14853, USA
2. CREOL, College of Optics and Photonics, University of Central Florida, Orlando, Florida 32816, USA

A laser is based on the electromagnetic modes of its resonator, which provides the feedback required for oscillation¹⁻². Enormous progress has been made in controlling the interactions of longitudinal modes in lasers with a single transverse mode. For example, the field of ultrafast science has been built on lasers that lock many longitudinal modes together to form ultrashort light pulses³. However, coherent superposition of many longitudinal *and* transverse modes in a laser has received little attention. The multitude of disparate frequency spacings, strong dispersions, and complex nonlinear interactions among modes greatly favor decoherence over the emergence of order. Here we report the locking of multiple transverse and longitudinal modes in fiber lasers to generate ultrafast spatiotemporal pulses. We construct multimode fiber cavities using graded-index multimode fiber (GRIN MMF). This causes spatial and longitudinal mode dispersions to be comparable. These dispersions are counteracted by strong intracavity spatial and spectral filtering. Under these conditions, we achieve spatiotemporal, or multimode (MM), mode-locking. A variety of other multimode nonlinear dynamical processes can also be observed. Multimode fiber lasers thus open new directions in studies of three-dimensional nonlinear wave propagation. Lasers that generate controllable spatiotemporal fields, with orders-of-magnitude increases in peak power over existing designs, should be possible. These should increase laser utility in many established applications and facilitate new ones.

The modes of a laser resonator are three-dimensional (3D) functions that vary along the axis of the resonator as well as in the two transverse dimensions (examples are illustrated in Fig. 1). Each mode has a distinct resonant frequency (Fig. 1b, d). In many cases of interest the 3D modes are separable into so-called longitudinal and transverse modes. A laser can oscillate in a superposition of these modes. If the relative phases of the modes are not controlled, the output is an incoherent spatiotemporal field that results from random interference. The modes can interact with each other in the gain medium and other components of a laser. An example that was recognized early in the study of lasers is the interaction of longitudinal modes with the population inversion, which underlies spiking temporal dynamics².

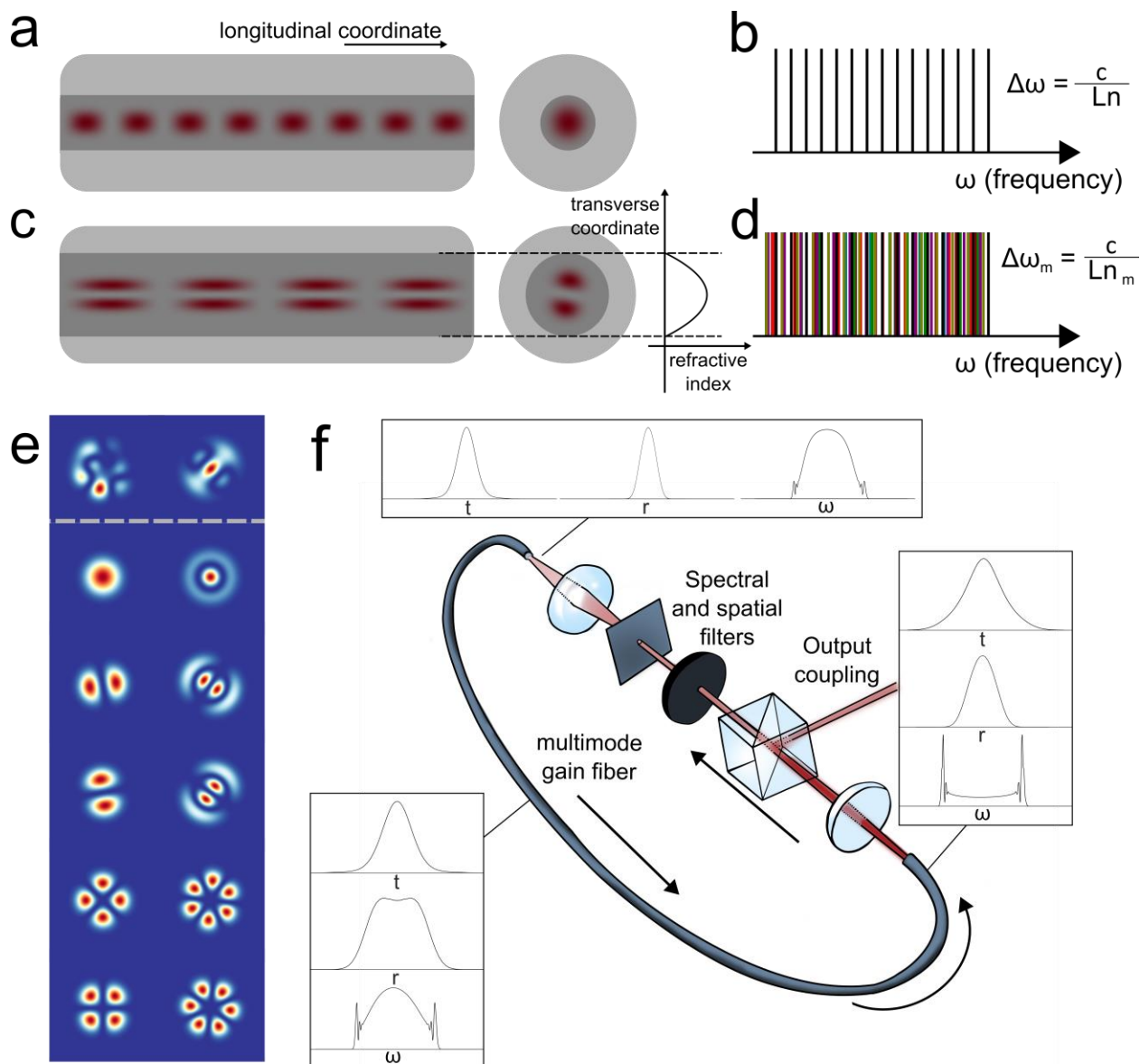


Figure 1: Conceptual outline of mode-locked multimode fiber lasers. **a-b.** In a conventional single transverse mode laser such as formed with a single-mode fiber, lasing occurs in longitudinal eigenmodes, which correspond to different patterns of the field along the length of the fiber, with identical transverse profiles and equally-spaced resonant frequencies. Nonlinear interactions between different longitudinal modes can cause them to establish a stable phase relationship known as mode-locking. This coherence, or synchronization, manifests as a circulating ultrashort pulse whose temporal shape is determined by the amplitudes of the contributing eigenmodes. **c-e.** In a multimode fiber, the resonant frequency spectrum (**d**) and transverse field distribution (two examples shown at the top of **e**) can be much more complex than in a single transverse mode laser. All possible field distributions can be decomposed into contributions from the numerous transverse eigenmodes (lower part of **e**). In a multimode fiber cavity, the lasing eigenmodes therefore describe a wide variety of three-dimensional electromagnetic field patterns. Each transverse mode corresponds to a family of equally-spaced longitudinal eigenmodes (different colors in **d**). One 3D mode is illustrated in **c**. **f.** In a suitably-designed cavity, mode-locking can arise among these 3D modes, manifested in the form of ultrashort circulating pulses with spatiotemporal shapes determined by the component 3D eigenmodes.

The situation can be simplified greatly by restricting operation to a single transverse mode. In addition, most applications benefit from the spatial coherence guaranteed by a single transverse mode, which underlies the minimum beam divergence and focused spot size. With the exception of high average power, the best performance for virtually all laser parameters -- ultranarrow emission spectra, ultrashort pulse duration, ultralow noise, *e.g.* -- is achieved through lasing in a single transverse mode. Operation in multiple spatial modes, by contrast, leads to significant theoretical and conceptual complexity. It is nonetheless widely employed in commercial lasers. These lasers can be cost-effective and reach very high average power, for applications that do not require high temporal or frequency precision, diffraction-limited propagation or focusing.

Highly-refined techniques have been developed to control the longitudinal modes of a laser. The number of oscillating modes can be as few as one, to more than one million perfectly-synchronized modes in a frequency comb³. Considering the exquisite control of the electromagnetic field achieved in lasers with a single transverse mode, the lack of attention paid to higher-dimensional coherent lasing states is conspicuous, if understandable. Reduction of the number of modes, which is analogous to reduction of temperature in thermodynamics, allows coherent interactions to be harnessed, similar to the observation of coherent quantum phenomena at ultralow temperatures. Highly-multimode operation corresponds to high temperature and entropy. Early works did propose locking of the 3D modes, under the special conditions that the resonant frequencies of different mode families were precisely aligned with one another. Mode-locking of this kind was initially demonstrated with a few modes^{4,5}, and has since been observed with two transverse modes of a femtosecond Ti:sapphire laser⁶. Spatiotemporal aspects of Kerr-lens mode-locking have meanwhile been treated as perturbations of a laser operating in a single transverse mode⁷⁻⁸.

Recent years have seen increased interest in 3D lasers⁸⁻¹⁷. Most notably, the random laser⁹⁻¹³ has brought many new perspectives on the physics of lasers. At the same time, interest in nonlinear multimode propagation has grown¹⁷⁻²⁴, both in anticipation of spatial division multiplexing²⁴ for telecommunications, and as a platform for high-power and/or new frequency fiber laser sources. For fundamental laser science, multimode fiber lasers offer many useful features compared to random lasers. The long active medium permits high gain and high nonlinearity, so that complex nonlinear dynamics can be expected. Propagation in a laser resonator can be more-controlled, through the use of saturable absorbers and spectral and spatial filters. While evidence for mode-locking behavior in selectively-pumped random lasers has been reported¹¹, the nonlinear dynamics, and in turn any coherent self-organization, are necessarily limited by the low nonlinearity and gain of random lasers.

Here we employ principles of normal-dispersion mode-locking²⁶⁻²⁷ in space and time – strong spectral and spatial filtering in addition to the high nonlinearity, gain and spatiotemporal dispersion of the fiber medium – to achieve spatiotemporal mode-

locking. The self-organized, mode-locked pulses take a variety of spatiotemporal shapes consisting of many spatial and longitudinal modes.

Results

We began our study by designing a cavity that would support highly-MM mode-locking at conveniently-low pump powers. To achieve spatiotemporal mode-locking, spatial and spectral filtering are required, and for low-power operation, the nonlinearity of the laser must be deliberately high. We accomplish this by using a few-mode gain fiber (10 μm diameter, supporting ~ 3 spatial modes), and placing a highly-MM GRIN fiber after the gain fiber, where the intracavity pulse energy and power are the highest. Highly-multimode excitation of the GRIN fiber is accomplished by fusing the two fibers with varying spatial offsets. This cavity is readily-modelled by a set of coupled nonlinear Schrödinger equations (NLSEs), and so serves as a convenient experimental and theoretical test-bed for multimode laser dynamics. Simulations reveal a rich variety of stable spatiotemporal pulses (examples shown in Figure 2, Supplementary Figure 1-10). These pulses form from noise and take on a variety of different modal compositions.

The straightforward emergence of stable spatiotemporal mode-locking is surprising, but can be understood through the comparable dispersion of spatial and longitudinal modes in GRIN fiber-based cavities, and the periodic spatial and spectral filtering we employ in the cavity. The formation and stability of these 3D mode-locked pulses is conceptually similar to 1D dissipative solitons and self-similar pulses in single-mode fiber²⁶⁻²⁷. In these lasers, normal dispersion and nonlinear phase modulation lead to a chirped pulse whose duration and bandwidth grows through most of the cavity. Strong spectral filtering of this chirped pulse reduces the duration and bandwidth, and so allows the pulse to meet the periodic boundary condition of the laser. In the current study, this approach is applied in space-time: in the multimode cavities, the combination of spatial and spectral filtering helps to establish a 3D steady-state pulse evolution with periodic boundary conditions in both space and time (Supplementary Figure 5-6, 15), a crucial aspect of mode-locking. Since in GRIN fiber the magnitude of spatial mode dispersion is similar to the chromatic (longitudinal mode) dispersion, coupling between all types of modes is likely. Hence in general mode-locking in such a 3D cavity involves numerous families of spatial modes.

Experimentally, spatial and spectral filtering are implemented through the overlap of the MM field with the gain fiber input, and a bandpass interference filter (Supplementary Video 1, Supplementary Figure 11). With suitable adjustments of the filters and waveplates (an experimental algorithm is described in the methods), a remarkable range of MM mode-locking states with substantial spatiotemporal self-organization can be observed (Figure 2, and Supplementary Figures 12-13, 28-39). Similar to the simulations, mode-locking may emerge from a highly multimode (~ 10 -100 spatial modes) CW lasing state, and form pulses with different spatiotemporal compositions (~ 10 or more spatial modes) (Fig. 2). We observe stable pulse trains with pulse

energies from 5 to 40 nJ, corresponding to routinely-available pump powers, and peak powers well below the threshold for end-facet damage.

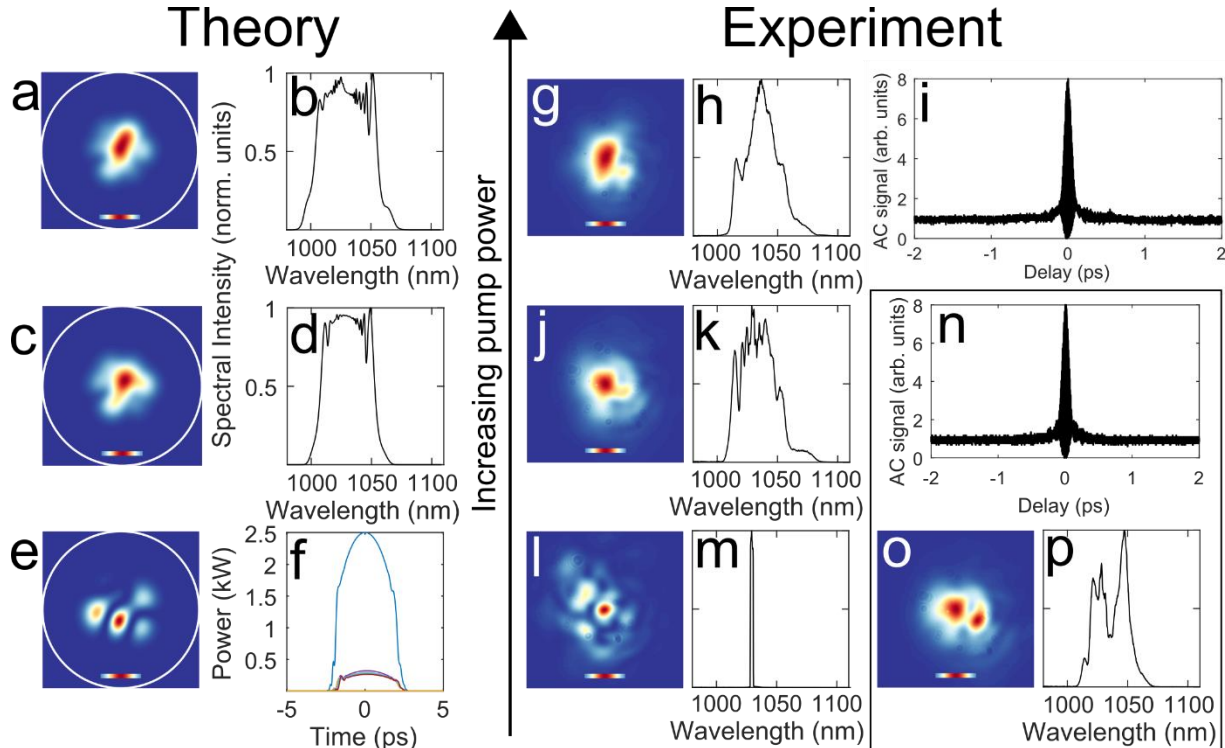


Figure 2: Spatiotemporal mode-locking in a laser cavity comprising few-mode gain fiber and highly-multimode passive GRIN fiber. **Numerical results a-f.** **a, c.** steady-state beam profile for simulation of a typical cavity for different gain saturation energies, **b, d.** corresponding total spectrum, averaged over 75 round trips. **e.** typical speckled beam profile expected for continuous wave lasing in the 10 modes considered in the simulations. **f.** mode-resolved temporal intensity profile corresponding to **c-d** (different traces are different spatial modes). The pulse's ~ 14 -nJ energy is comprised of ~ 8.5 nJ in the fundamental mode, and 1 nJ in the next 6 higher-order modes. A wide variety of pulses with different modal compositions are observed; other numerical examples and further details shown in Supplementary Figures 1-10. **Experimental results g-p.** **g-i** show the beam profile, spectrum (linear scale) and autocorrelation of the dechirped pulse for a given cavity configuration. **j-m** show the beam profile and spectrum for the output field for decreasing pump power for the same cavity configuration. This sequence, along with **a-f**, illustrates the spatiotemporal transition to mode-locking from a highly-multimode continuous wave lasing state with increasing pump power, and the spatiotemporal changes that occur as pump power is further increased beyond the mode-locking threshold. The simulation and experimental results are not directly comparable, since the simulation considers only 10 of the >100 modes in the experiment, and because the experimental fiber-fiber mode coupling coefficients are not precisely known. When the cavity alignment is adjusted, different multimode pulses can be observed (**n-p**). The scale bar on beam profiles shows the Gaussian intensity of the fundamental mode ($13 \mu\text{m}$ mode-field diameter).

Informed by results from the low-power cavity, we investigated high-power spatiotemporal mode-locking in a cavity based completely on a partially-graded, highly multimode gain fiber. With high power and strong spectral and spatial filtering, we observe many different complex spatiotemporal dynamics in numerical simulations

(Supplementary Figures 15-21), including stable mode-locked pulse trains. Figure 3 shows a representative example, where we investigate high power scaling by slowly incrementing the gain saturation energy of the fiber (this mimics the gradual adjustment of pump power in experiments). This example shows three distinct regimes of spatiotemporal mode-locking with increasing pulse energy. At relatively low powers, a multimode mode-locked pulse forms. At higher energy (Fig. 3b) the field undergoes a spatiotemporal transition, suddenly exhibiting oscillatory mode-locking with periods longer than the cavity repetition period. At still higher energies, the field transitions into a Gaussian spatial mode (see Supplementary Figure 15, 20-21 for steady-state operation and peak-power scaling).

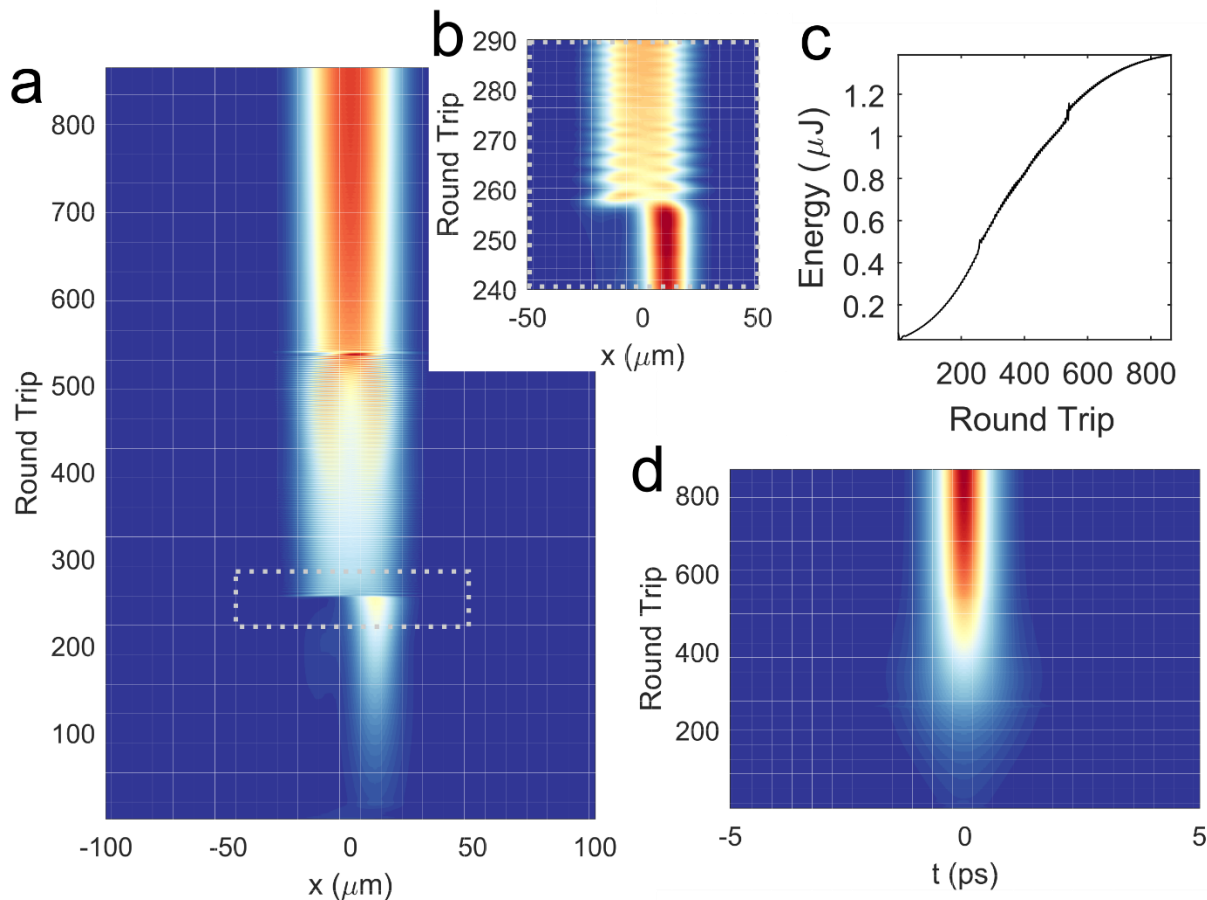


Figure 3: Numerical simulation showing different spatiotemporal mode-locking regimes in an all-multimode fiber cavity. A simplified spatiotemporal GNLSE (see methods, Supplementary Information) models the system. A stable pulse is launched into the cavity and the saturation energy is increased by 5% every 6 round trips. **a.** The output spatial profile (**b.** zoom on transition area). **c.** Energy as a function of round trip, and **d.** temporal profile for increasing round trip. The steady-state intracavity pulse evolution corresponding to fixed gain saturation energy at the highest level shown here is plotted in Supplementary Figure 15.

We constructed a corresponding laser similar to the previously-described cavity, except all of the fiber is highly-multimode, quasi-GRIN gain fiber, and spatial filtering is

supplemented by an adjustable slit or iris (Figure 1f, methods, Supplementary Figure 22). Above a threshold pump power, spatiotemporally self-organized, mode-locked lasing states are observed (Figure 4). As the pump power is adjusted, we observe discontinuous changes in the field's spatial, temporal and spectral properties, a strong signature of the transition between highly-spatially-multimode (~ 10 -100 modes) continuous-wave (CW) lasing and multimode mode-locking (~ 2 -10 modes). Different mode-locked states are observed for different cavity configurations (Supplementary Figure 25), but the minimum peak power for which mode-locking occurs in this highly-multimode laser is ~ 1 MW. Consequently, systematic exploration of this laser and future engineering of practical instruments will require application of known techniques for avoiding fiber damage. As with the low-energy cavity, direct measurements of the 3D field will be an important step for increased understanding of spatiotemporal mode-locking. Ongoing developments in this direction are promising (e.g., Ref. 29), and we anticipate incorporation of such diagnostics in future work.

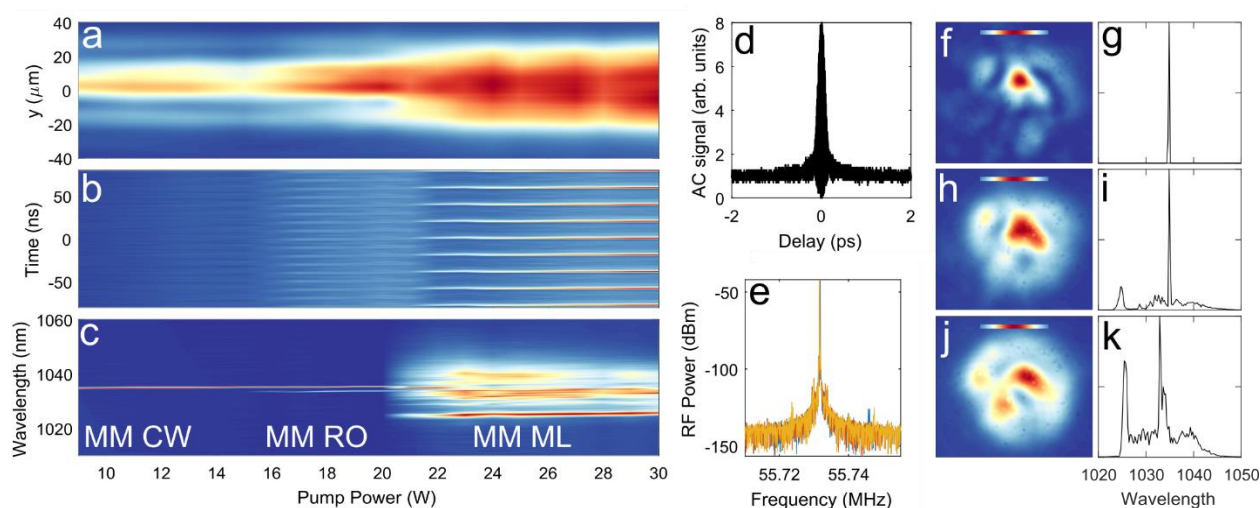


Figure 4: Spatiotemporal transition to mode-locking in an all-multimode fiber laser cavity. **a.** near-field beam profile integrated over 1 dimension, **b.** temporal variation of the output **c.** spectrum. As the pump power is reduced, the field transitions from pulsed mode-locking (MM STML, spectrum and beam profile shown in **j** and **k**), to bistability with relaxation oscillations (**h** and **i**), to relaxation oscillations (MM RO), to continuous wave operation (MM CW lasing, **f** and **g**). 9 W is the CW lasing threshold. Similar results are observed for increasing pump power (see methods for details). The coherence of the mode-locked state is evident from the autocorrelation of the dechirped pulse and the RF spectrum (**d** and **e**, see methods). The scale bar in **f, h, j** shows the Gaussian profile of the fundamental mode of the fiber. High-speed measurements of the STML and RO regimes are shown in Supplementary Figure 23-24.

Discussion

Investigation of 3D mode-locking will connect scientifically to areas well beyond short-pulse generation. The dimensionality and controllable dissipation and disorder make consideration of wave turbulence and condensation³⁰⁻³¹ especially interesting. With longer or suitably-designed fibers, disorder can be introduced controllably, thereby

bridging the gap to random lasers and allowing exploration of the entire parameter space of multimode lasing¹²⁻¹³. Although disorder is weak in the present work, recent research indicates that multimode self-organization may be robust to disorder^{20,21}. This will be important for applications, which will ultimately require environmental stability.

The potential of MM mode-locked lasers for applications is significant. While no attempt has been made to maximize performance yet, results obtained with the multimode cavity (150-nJ and 150-fs pulses, for ~1-MW peak power and ~10-W average power) already rival the best achieved with flexible, large-area single-mode fibers²⁸. The presence of inter- and intra-modal dispersions allows pulses to tolerate high nonlinear phase shifts without becoming unstable¹⁹. For greater pulse energies, we expect the emergence of a stable Gaussian output beam, which will be useful for most conventional applications. Since the size of MM waveguides may be considerably larger than LMA fibers (or rods) and the pulse is chirped inside the cavity, we expect scaling of pulse energy by over 2 orders of magnitude to be possible in principle. The ultimate performance will likely be limited by practical concerns – fiber damage, e.g. – rather than fundamental limits from nonlinear pulse distortions.

Exploration of the full scope of MM mode-locking will require developments on several fronts, including measurement capabilities. Despite the challenges, we expect the pay-off to be high. The ability to generate high-power and spatiotemporally-engineered coherent light fields should lead to breakthroughs in unexpected as well as expected areas.

Methods

Simulations – low power cavity

Simulations of this cavity are performed using the generalized multimode nonlinear Schrödinger equation¹⁸. Different combinations of modes are considered, and the dispersions and mode-coupling tensors are calculated from the numerically-calculated modes for an assumed GRIN fiber with a 50 μm diameter, refractive index power of 2.08, and numerical aperture of 0.2. The gain fiber is approximated as a single-mode fiber. The effective saturable absorber provided by nonlinear polarization rotation is modelled by an idealized saturable absorber applied to the composite single-mode field to be coupled into the single-mode fiber. Overlap between the gain and multimode fiber is controlled by two sets of mode coupling coefficients describing the excitation of modes at the splice point, along with the overlap of the MM output field with the gain fiber. The gain spectrum is modelled as a Gaussian with 40-nm bandwidth, the small-signal gain is 30 dB. Stable pulses are observed for a wide variety of parameters; more specific details and representative examples are provided in the supplementary information (Supplementary Figures 1-10).

In general, spatiotemporally mode-locked pulses exhibit spatiotemporal coupling, or dispersion. This is analyzed numerically in Supplementary Figures 34-39, and shown to be of negligible importance for the experimental results presented here.

Experiments – low power cavity

The low-power cavity (Supplementary Figure 11, Supplementary Video 1) was designed to support strongly spatially multimode mode-locking at low power levels. 1-2 m of 10- μm diameter step-index, weakly multimode gain fiber (Thorlabs YB1200-10/125DC) is spliced to 0.5-2 m of Corning OM4 graded-index multimode fiber. In order to excite many modes, the GRIN fiber is aligned offset from the gain fiber's center by up to 15 μm . In order to minimize reflections from this splice point, the arc fusion splicer is continuously arced until the fiber's claddings are overlapped to a high degree. This process strongly distorts several millimeters of GRIN fiber nearest the splice, ensuring that both highly-multimode excitation and low-loss coupling from the gain fiber into the multimode fiber occurs. Pump light leakage is controlled by application of index-matching gel and protection by darkened foil. In both cavities, bulk-optic filters, waveplates, isolators, and beamsplitters are employed in a $\sim 1\text{-m}$ long free-space section used for experimental convenience and power handling. In both cavities, the fiber is laid loosely with an approximate coiling diameter of 50 cm, and the fiber is pumped by a multimode, 30-W, 976-nm diode laser (Gauss Laser) through dichroic mirrors.

In order to achieve mode-locking in any cavity, intracavity back-reflections that lead to parasitic lasing must be suppressed. In a multimode cavity, this is particularly important since there are numerous paths for back-reflections to form and travel. To avoid this, careful optimization of the cleave parameters for the angle-cleaved fibers is performed. Similar optimization is required for splices, with MM-exciting splices performed as described above.

Mode-locking in the cavity is easily initiated, and different states are accessed by adjusting the waveplates and pump power, and by tuning the mirrors in the cavity to change the overlap between the multimode field that exits the GRIN fiber and the gain fiber. A wide variety of spectral filters and mirror alignments result in many different spatiotemporal pulses. However, strong Raman-based effects lead to pulse distortions and Q-switching, unless a filter with a single pass-band is used (commonly used birefringent filters support many passbands). Even with this measure, at high pump powers we regularly observe strong Raman-induced Q-switching, which limits the maximum pulse energy from this cavity.

Simulations – all multimode fiber cavity

Simulations are performed using a (2+1)-D generalized nonlinear Schrödinger equation with spatially-saturating gain and spatiotemporal saturable absorption (details in Supplementary Information Section 3). This models the most important physical

processes in the oscillator qualitatively, and allows simulations of many round-trips and meters of fiber to be performed in reasonable times. For these simulations, the saturable absorber is an idealized saturable absorber applied point-by-point to the full spatiotemporal electric field envelope. The gain is modelled similarly to standard fiber techniques, except that saturation is dependent on the spatially-varying, time-integrated intensity in order to properly account for gain competition. For the results shown in Figure 3, the cavity comprises a 50 cm gain fiber with a 1D index profile similar to the MM fiber used in experiments. A 50 μm Gaussian (all bandwidths listed are full-width-at-half-maximum) spatial filter and 30 nm Gaussian spectral filter are applied to the spatiotemporal field envelope after saturable absorption and output coupling. The gain spectrum is modelled as a Gaussian with 40 nm bandwidth, and the small signal gain is taken to be 25 dB. The modulation depth of the saturable absorber is taken to be 100%, although stable pulses are observed for lower values. The output coupling ratio is taken to be 90%, and a lumped loss from fiber coupling of 50% is applied once per roundtrip. The dispersion of the fiber is assumed to be 20 fs²/mm.

Experiments – all-multimode cavity

The all-multimode, or high-power, cavity (Supplementary Figure 22) employs Yb-doped multimode fiber with a partially-graded index profile (Nufern FUD-7005) shown in Supplementary Figure 14. This fiber supports roughly 90 spatial (180 total) modes at 1030 nm, and the graded-index design leads to small modal dispersion compared to conventional step-index fibers. In order to maximize the nonlinear phase shift and achieve spatiotemporal mode-locking at modest pump powers, 3.5-4.0 m of this fiber are used – significantly more than would be required for an efficient laser cavity.

The cavity is initially aligned to maximize continuous wave lasing power without additional spectral or spatial filtering. The finite gain bandwidth and the field's overlap with the isolator aperture and the fiber input provide some spectral and spatial filtering, but for the powers considered here only unstable mode-locking can be achieved without stronger filtering. A single pass-band spectral filter (typically a simple interference filter, Thorlabs FLH1030-10) is then added and a spatial filter (an adjustable slit or pinhole) is closed until the intracavity field is noticeably clipped (the maximum power is generally reduced by 20%). Mode-locking can then be initiated and adjusted by rotating the waveplates. This procedure is generally enough to allow many mode-locked states, and provided the pump power is high enough, mode-locking is straightforward to observe. However, if mode-locking cannot be initiated with this method, the waveplates are adjusted until relaxation oscillations and/or self-Q-switching are evident from measurements of the spectrum or temporal profile with a fast photodetector. At this point, the spatial filter and folding mirrors can be adjusted slightly until mode-locking is observed.

Experiments – field measurements

The spectrum of the field exiting the multimode fiber is measured, after sampling by beamsplitters, by coupling it into a long highly multimode fiber connected to an optical spectrum analyzer. The long multimode fiber allows sampling of most of the field, and the long diffusive linear propagation serves to spatially-average the spectrum. In some cases, a single-mode fiber replaces the multimode fiber, in order to observe spatially-sampled spectra. The beam profile is measured using a 4-f telescope, where the first lens is aligned by imaging amplified spontaneous emission from the laser cavity onto the camera.

Our measurements confirm numerical predictions of self-organized, spatiotemporally mode-locked coherent pulses. When the spectrum of the mode-locked pulse is measured using a single-mode-fiber coupled optical spectrum analyzer, we observe changes in the spectrum as the beam is translated, which confirms the multimode spatiotemporal structure implied by spatial measurements and numerics. We measure the interferometric autocorrelation of pulses after dispersion compensation by a grating compressor. Use of two-photon absorption ensures that the entire spatiotemporal field is integrated into the measurement, without complex phase-matching¹⁹. The coherence of the pulses is confirmed by the fact that they can be dechirped to near their spectrum's transform limit, with an 8:1 peak:background ratio in their interferometric autocorrelation. Deviations from transform limit in the low-power cavity are sometimes observed, and these can be attributed to Raman scattering, which appears in the red side of the pulse spectrum for high pulse energies. Meanwhile, radio-frequency spectral measurements show >95 dB contrast between the mode-locked repetition frequency and the noise background, consistent with the value expected for stable mode-locking in oscillators with rigorously single spatial mode waveguides. Assessment of the peak power is significantly complicated by the complex spatiotemporal structure of the pulses. However, spectral broadening of sampled portions of the beam in single-mode fiber agree roughly with numerical simulations, and the observed single-pulse energy is consistent with the nonlinear phase shift inferred from the spectral breathing of the pulse in the cavity (for further details, see Supplementary Figures 26-33 and accompanying discussion).

To measure the spatiotemporal mode-locking transition, we choose to decrease the pump power starting from the highest value. After measurements are made for decreasing pump power, the power is returned to the original level. For all results shown here and in the Supplementary Information, nearly identical mode-locking is recovered. In other words, the mode-locked states observed here are self-starting. However, for increasing pump powers we generally observe poorer stability of the mode-locked state. In the all-multimode cavity, peak power-related end facet damage is regularly observed during the instability of mode-locked states. To avoid fiber damage we therefore performed detailed measurements with decreasing pump power in experiments.

Acknowledgements

We thank Nufern for providing the partially-graded multimode gain fiber, Walter Fu for pointing this product out, Zachary Ziegler for discussions and contributions to some of

the numerical codes used for MMGNLSE simulations, Zhanwei Liu for discussions and his early contribution to the work, Emily Falco for the laser schematic in Figure 1d, and Will Renninger for his critical review of an early version of the manuscript.

Funding

Office of Naval Research grant N00014-13-1-0649

National Sciences Foundation grant ECCS-1609129

References

1. Schawlow, A. L. & Townes, C.L. Infrared and optical masers, *Phys. Rev.* **112** (6), 1940 (1958).
2. Mocker, H. W., & Collins, R. J. Mode competition and self-locking effects in a Q-switched ruby laser, *Appl. Phys. Lett.* **7** (10), 270-273 (1965).
3. Cundiff, S.T. & Ye, J. Colloquium: Femtosecond optical frequency combs, *Rev. Mod. Phys.* **75**, 325 (2003).
4. Auston, D. Transverse mode locking. *IEEE J. Quant. Electron* **4** (6), 420-422 (1968).
5. Smith, P.W. Simultaneous phase-locking of longitudinal and transverse laser modes, *Appl. Phys. Lett.* **13**, 235 (1968).
6. Côté, D., & van Driel, H. M. Period doubling of a femtosecond Ti: sapphire laser by total mode locking, *Opt. Lett.* **23** (9), 715-717 (1998).
7. Christov, I.P., Kapteyn, H.C., Murnane, M. M., Huang, C.-P. & Zhou, J. Space-time focusing of femtosecond pulses in a Ti:sapphire laser, *Opt. Lett.* **20**, 309 (1995).
8. Jirauschek, C., Kärtner, F.X. & Morgner, U. Spatiotemporal Gaussian pulse dynamics in Kerr-lens mode-locked lasers, *J. Opt. Soc. Am. B* **20**, 1356-1368 (2003).
9. Cao, H., Zhao, Y. G., Ho, S. T., Seelig, E. W., Wang, Q. H., & Chang, R. P. H. Random laser action in semiconductor powder, *Phys. Rev. Lett.* **82** (11), 2278 (1999).
10. Wiersma, D. S. The physics and applications of random lasers. *Nat. Phys.* **4** (5), 359-367 (2008).
11. Leonetti, M., Conti, C., & Lopez, C. The mode-locking transition of random lasers. *Nat. Photon.* **5** (10), 615-617 (2011).
12. Conti, C., Leonetti, M., Fratilocchi, A., Angelani, L., & Ruocco, G. Condensation in disordered lasers: Theory, 3 D+ 1 simulations, and experiments. *Phys. Rev. Lett.* **101** (14), 143901 (2008).
13. Antenucci, F., Crisanti, A., Ibáñez-Berganza, M., Marruzzo, A., & Leuzzi, L. Statistical mechanics models for multimode lasers and random lasers. *Philos. Mag.* **96** (7-9), 704-731 (2016).
14. Guenard, R. *et al.* 2017. Kerr self-cleaning of pulsed beam in an ytterbium doped multimode fiber. *Opt. Express* **25** (5), 4783-4792 (2017).

15. Renninger, W.H. & Wise, F.W. Spatiotemporal soliton laser, *Optica* **1**, 101-104 (2014).
16. Nixon, M., Katz, O., Small, E., Bromberg, Y., Friesem, A. A., Silberberg, Y., & Davidson, N. Real-time wavefront shaping through scattering media by all-optical feedback. *Nat. Photon.* **7** (11), 919-924 (2013).
17. Nazemosadat, E. & Mafi, A. Nonlinear switching in multicore versus multimode waveguide junctions for mode-locked laser applications. *Opt. Express* **21**, 30739–45 (2013).
18. Poletti, F. & Horak, P. Description of ultrashort pulse propagation in multimode optical fibers. *J. Opt. Soc. Am. B* **25**, 1645-1654 (2008).
19. Wright, L. G., Renninger, W. H., Christodoulides, D. N. & Wise, F. W. Spatiotemporal dynamics of multimode optical solitons. *Opt. Express* **23**, 3492–506 (2015).
20. Krupa, K. *et al.* Spatial beam self-cleaning in multimode fibre. *Nat. Photon.* (2017).
21. Lopez-Galmiche, G., *et al.* Visible supercontinuum generation in a graded index multimode fiber pumped at 1064 nm. *Opt. Lett.* **41** (11), 2553-2556 (2016).
22. Pourbeyram, H., Agrawal, G. P. & Mafi, A. Stimulated Raman scattering cascade spanning the wavelength range of 523 to 1750 nm using a graded-index multimode optical fiber. *Appl. Phys. Lett.* **102**, 201107 (2013).
23. Hellwig, T., Walbaum, T., & Fallnich, C. Optically induced mode conversion in graded-index fibers using ultra-short laser pulses. *Appl. Phys. B*, **112** (4), 499-505 (2013).
24. Demas, J., Steinvurzel, P., Tai, B., Rishøj, L., Chen, Y., & Ramachandran, S. Intermodal nonlinear mixing with Bessel beams in optical fiber. *Optica*, **2** (1), 14-17 (2015).
25. Richardson, D. J., Fini, J. M. & Nelson, L. E. Space-division multiplexing in optical fibres. *Nat. Photon.* **7**, 354–362 (2013).
26. Renninger, W. H., Chong, A., & Wise, F. W. Pulse shaping and evolution in normal-dispersion mode-locked fiber lasers. *IEEE J. Sel. Top. Quantum Electron.*, **18** (1), 389-398 (2012).
27. Chong, A., Wright, L. G., & Wise, F. W. Ultrafast fiber lasers based on self-similar pulse evolution: a review of current progress. *Rep. Prog. Phys.*, **78** (11), 113901 (2015).
28. Baumgartl, M., Ortaç, B., Lecaplain, C., Hideur, A., Limpert, J., & Tünnermann, A. Sub-80 fs dissipative soliton large-mode-area fiber laser. *Opt. Lett.*, **35** (13), 2311-2313 (2010).
29. Guang, Z., Rhodes, M., Davis, M., & Trebino, R. Complete characterization of a spatiotemporally complex pulse by an improved single-frame pulse-measurement technique. *J. Opt. Soc. Am. B*, **31** (11), 2736-2743 (2014).

30. Picozzi, A. *et al.* Optical wave turbulence: Towards a unified nonequilibrium thermodynamic formulation of statistical nonlinear optics. *Phys. Rep.*, **542** (1), 1-132 (2014).
31. Turitsyna, E. G. *et al.* The laminar-turbulent transition in a fibre laser. *Nat. Photon.* **7** (10), 783-786 (2013).

Supplementary Information for 'Spatiotemporal mode-locking in multimode fiber lasers'

Logan G. Wright¹, Demetrios N. Christodoulides², and Frank W. Wise¹

1. School of Applied and Engineering Physics, Cornell University, Ithaca, New York 14853, USA
2. CREOL, College of Optics and Photonics, University of Central Florida, Orlando, Florida 32816, USA

CONTENTS

Supplementary simulation details and results for the low-power multimode cavity	16
Supplementary experimental details and results for the low-power multimode cavity.....	28
Supplementary simulation details and results for the all-multimode cavity.....	31
Supplementary experimental details and results for the all-multimode cavity	40
Peak power assessment.....	42
Approach 1: spectral broadening in single-mode fiber	42
Approach 2: analytic estimate of intracavity nonlinear phase shift	46
Discussion of spatiotemporal dispersion/coupling in spatiotemporally mode-locked pulses	47
Supplementary References.....	52

SUPPLEMENTARY SIMULATION DETAILS AND RESULTS FOR THE LOW-POWER MULTIMODE CAVITY

We performed numerical simulations of the low-power multimode cavity using the GMMNLSE to describe evolution on the modal field envelopes, $A_p(z, t)$, in the passive multimode GRIN fiber:

$$\begin{aligned} \partial_z A_p(z, t) = & i \left(\beta_0^{(p)} - \Re[\beta_0^{(0)}] \right) A_p - \left(\beta_1^{(p)} - \Re[\beta_1^{(0)}] \right) \frac{\partial A_p}{\partial t} + \sum_{m=2}^3 i^{m+1} \frac{\beta_m}{m!} \partial_t^m A_p \\ & + i \frac{n_2 \omega_0}{c} \left(1 + \frac{i}{\omega_0} \partial_t \right) \sum_{l,m,n} \{ (1 - f_R) S_{plmn}^k A_l A_m A_n^* \\ & + f_R A_l S_{plmn}^R \int_{-\infty}^t d\tau A_m(z, t - \tau) A_n^*(z, t - \tau) h_R(\tau) \} \end{aligned}$$

The parameters are defined in Supplementary Reference 1. For the examples shown here, the spatial modes are numerically calculated assuming linear polarization at a wavelength of 1030 nm, and the dispersion parameters are obtained by polynomial fits of the dispersion curves obtained by numerically solving for the modes from ~ 1550 nm to ~ 750 nm. We approximate the propagation in the few-mode gain fiber by a single mode GNLSE in the fundamental mode of that fiber.

At the interface between the gain fiber and the multimode (MM) fiber, and between the MM fiber and the gain fiber, we approximate the MM excitation and the spatial filtering process by projection coefficients, P_{1p} and P_{2p} , where p is the index of the mode, running from 1 to 10 for the simulations shown here. That is, the field entering the MM fiber is:

$$A_p(z = 0, t) = P_{1p} A_{SMF}(z = L_{SMF}, t)$$

The field that re-enters the gain fiber is

$$A_{SMF}(z = 0, t) = \sum_{p=1}^N P_{2p} A_p(z = L_{MMF}, t)$$

In both cases, the field is re-normalized so that the projection conserves energy. After output from the MM fiber, the transformation above is applied and an ideal Gaussian spectral filter is applied. Then a saturable absorber transfer function is applied to the field:

$$A(z, t) \rightarrow A(z, t) \sqrt{1 - \frac{\text{mod_depth}}{1 + \frac{|A(z, t)|^2}{I_{sat}}}}$$

A portion of the field is taken as the output, and a lumped loss (50% unless otherwise stated) is applied before the field is propagated through the gain fiber again. The application of the saturable absorber to the projected single-mode field is a significant simplification over the

spatiotemporal saturable absorption which occurs in the experiments (although some of this latter effective saturable absorption, which acts like a generalized Kerr lens, is still included). More systematic and rigorous numerical and theoretical models for both cavities will be described in a future report, and a subsequent section here details simulations using spatiotemporal saturable absorption and multimode gain fiber.

The following figures show representative examples of multimode mode-locking. Due to the nature of the multimode excitation by offset splicing, and the overlap of the multimode field with the weakly-multimode gain fiber input, we expect that the fundamental mode and other radially-symmetric modes are predominantly excited. All simulations were seeded with random noise along with a pulse with amplitude 30% higher than the noise and placed at -15 ps, to encourage formation of a pulse at that point in the temporal window of the simulation. The spatial profile of the initial noise field launched into the simulation is plotted in the upper left-hand corner of the following plots, to provide a frame of reference for how spatially-multimode the cavity is.

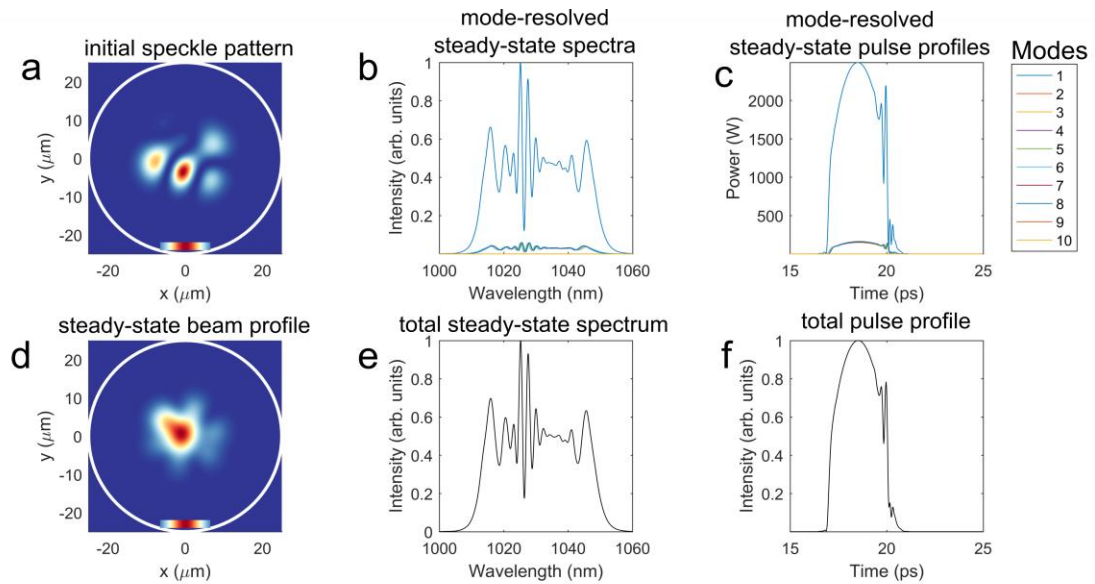
The first two examples show typical output fields where the fundamental mode is the highest-power spatial mode. The second shows a common feature of multimode mode-locking, namely the appearance of spectral fringes on the blue side of the center of the pulse spectrum.

Supplementary Figures 1-2, and **Supplementary Figures 3-4** show two examples of typical output fields where the fundamental mode is the highest-power spatial mode.

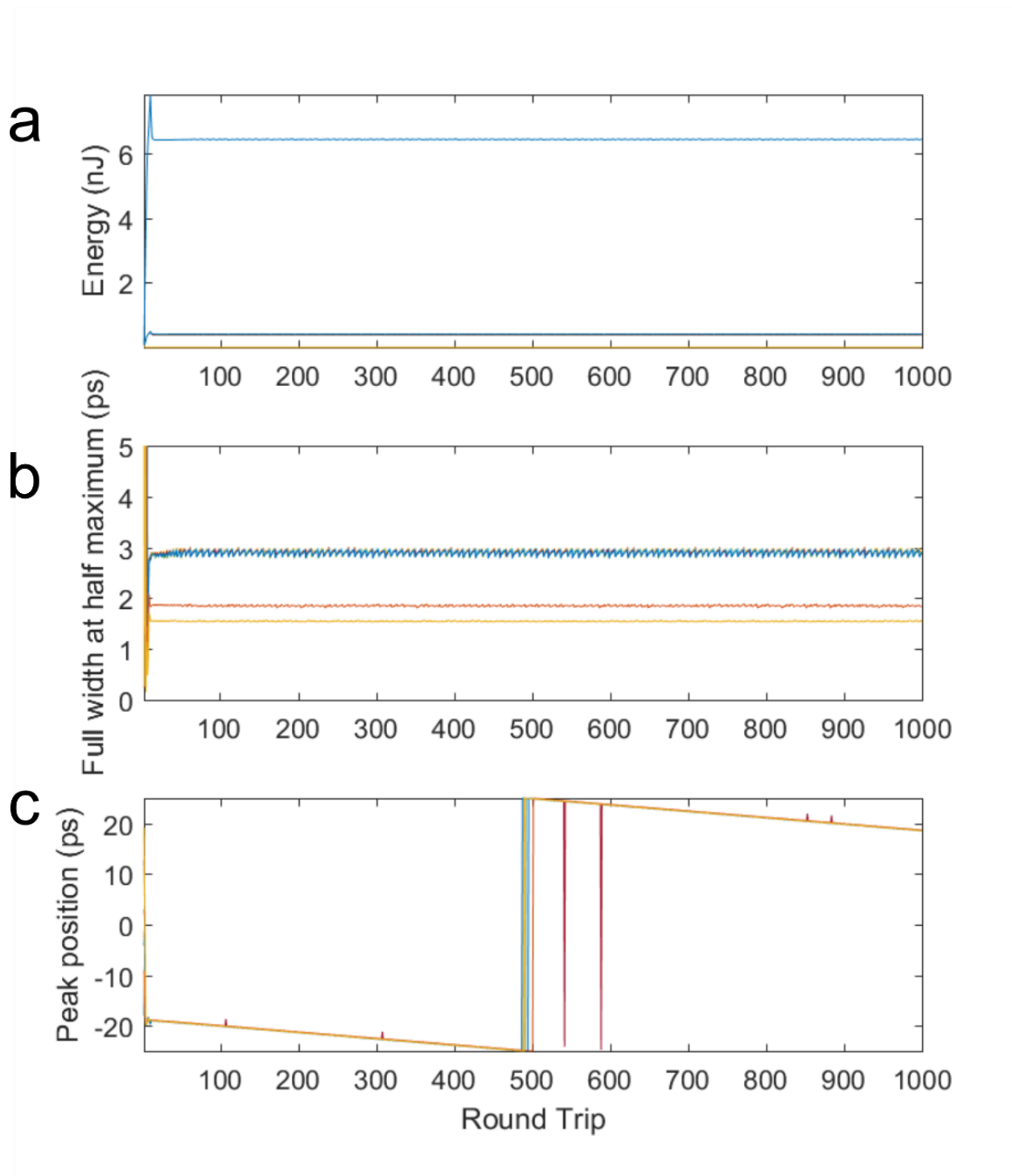
Supplementary Figures 1-2 shows a common feature of multimode mode-locking, the appearance of spectral fringes near the center of the pulse spectrum.

Supplementary Figures 5-6 show the intracavity evolution of the pulse, starting from noise, and at steady-state, corresponding to **Supplementary Figures 3-4**. *These illustrate the basic principles of spatiotemporal mode-locking in this oscillator, and so these are among the most important results presented in this Supplementary Information document.* Qualitatively similar intracavity evolutions are observed for other states.

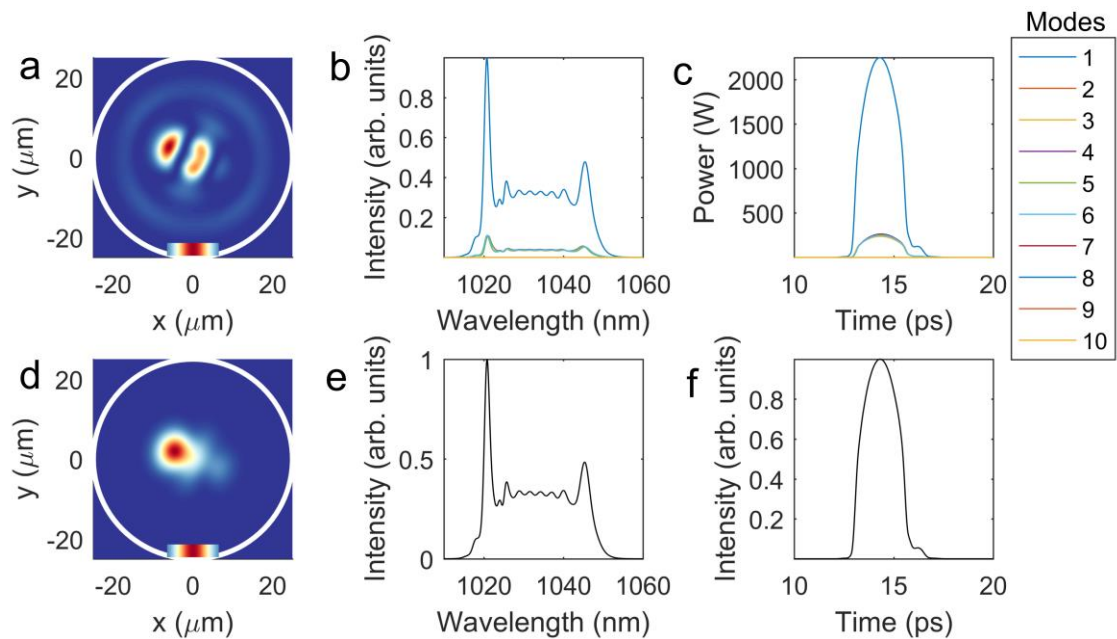
Supplementary Figures 7-10 show the possibility of multimode mode-locking with many modes having similar amplitudes, and with a higher-order mode carrying most of the power. These demonstrate the range of spatiotemporal pulses possible, and so provide some support for future applications in versatile 3D ultrafast pulse generation.



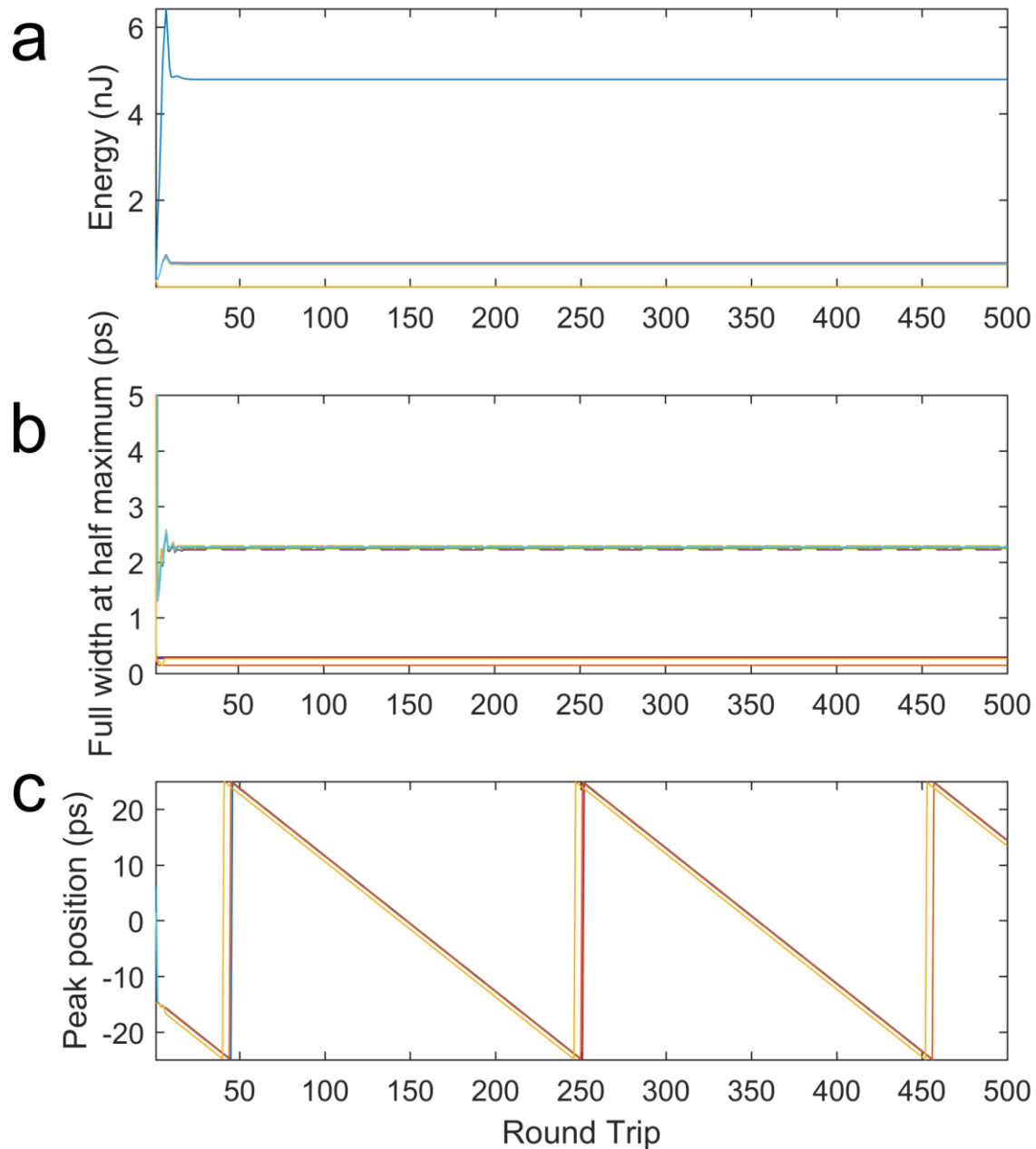
Supplementary Figure 1: Typical numerical result of multimode mode-locking with strong fundamental mode content. From top left to bottom right: **a.** Initial spatial output profile, **b.** mode-resolved steady state spectra, and **c.** mode-resolved pulse intensity, **d.** steady-state output spatial profile, **e.** total steady-state spectrum and **f.** pulse intensity. The scale bars show the Gaussian intensity distribution of the fundamental mode, and the white circle indicates the fiber core. The legend in the upper right corner refers to the mode-resolved plots **b-c.** Here the 10 modes correspond to the first 10 lowest order modes of the fiber. The output coupling ratio is 70%, the modulation depth is 100% (with a saturation power 2 kW), the filter bandwidth is 9 nm, the saturation energy is 3 nJ, and the passive (gain) fiber length is 50 (150) cm. The projection coefficients for passive fiber to gain fiber and from gain to passive fiber are both set to $[4 \ 1 \ 1 \ 1 \ 1 \ 1 \ 1 \ 1 \ 0 \ 0]$ (the coefficients are subsequently normalized so that their total magnitude is 1 to conserve energy at each fiber transition). The pulse is stable, but exhibits a slight oscillatory behavior indicative of some intermode beating (visible as modulation near the center of the spectrum, and on the edge of the pulse).



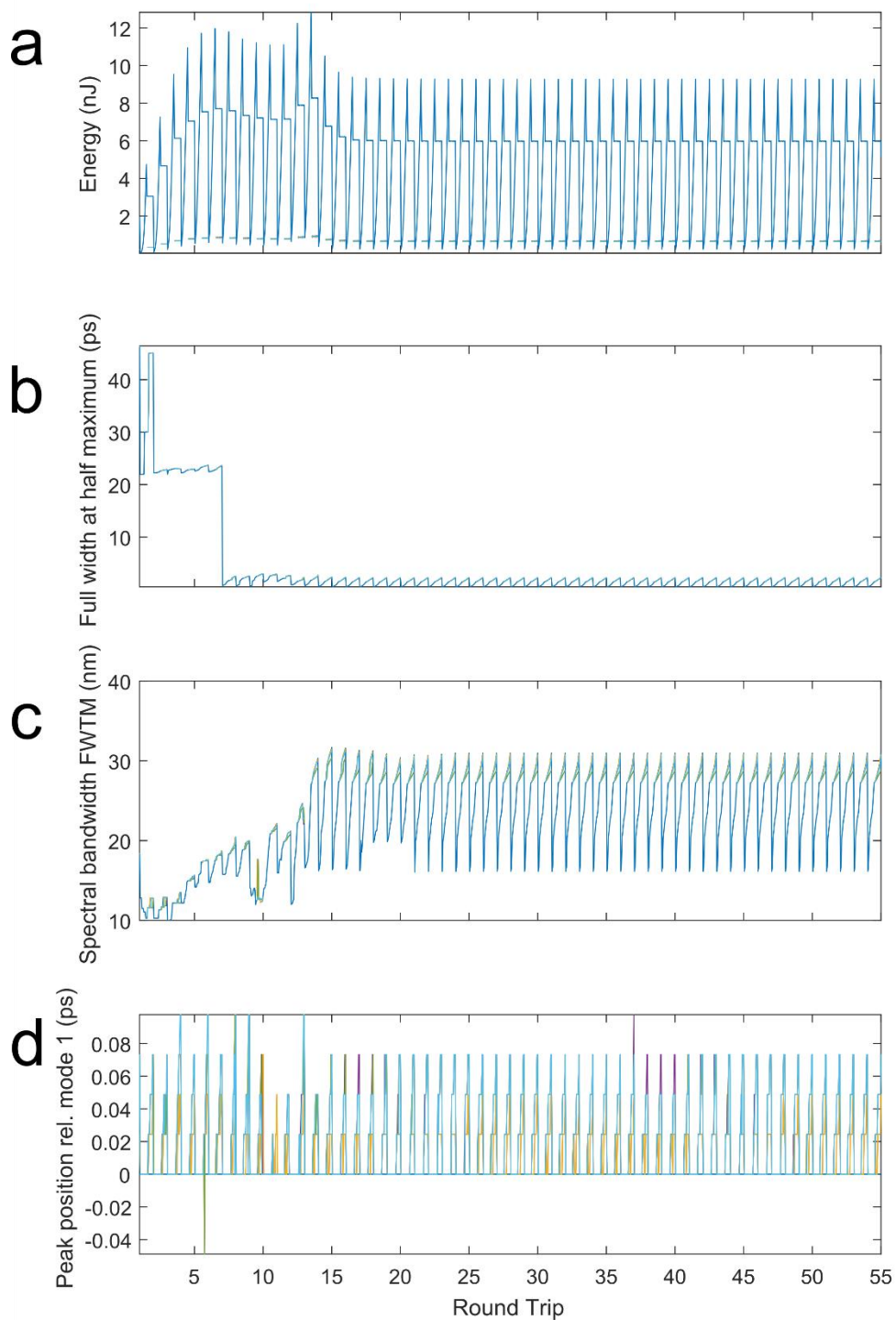
Supplementary Figure 2: Evolution of the field in the multimode cavity. Numerical results corresponding to **Supplementary Figure 1**. The plots show the **a.** output pulse energy, **b.** duration, and **c.** the position of the pulse in time. The mode-locked pulses' properties are stable over many round trips and do not oscillate from round trip to round trip. Due in part to its spatially-multimode nature, the mode-locked pulse moves at a finite group velocity relative to the simulation window, which moves at the velocity of the fundamental mode. Some numerical artifacts are present in the bottom plot due to this motion (at 500-600 round trips), but these do not affect the stable pulse evolution.



Supplementary Figure 3: Typical numerical example of fundamental-mode dominant multimode mode-locking in the low-energy cavity. From top left to bottom right: **a.** Initial spatial output profile, **b.** mode-resolved steady state spectra, and **c.** mode-resolved pulse intensity, **d.** steady-state output spatial profile, **e.** total steady-state spectrum and **f.** pulse intensity. The scale bars show the Gaussian intensity distribution of the fundamental mode, and the white circle indicates the fiber core. The legend in the upper right corner refers to the mode-resolved plots **b-c.** The simulated modes are the first 6 lowest order modes, while modes 7-10 correspond to higher-order radially-symmetric modes which are expected to be predominantly excited. The output coupling ratio is 80%, the modulation depth is 99% (with a saturation power 4 kW), the filter bandwidth is 9 nm, the saturation energy is 3 nJ, and the passive (gain) fiber length is 50 (150) cm. The projection coefficients for passive fiber to gain fiber and from gain to passive fiber are both set to [3 1 1 1 1 1 0 0 0] (the coefficients are subsequently normalized so that their total magnitude is 1 to conserve energy at each fiber transition).

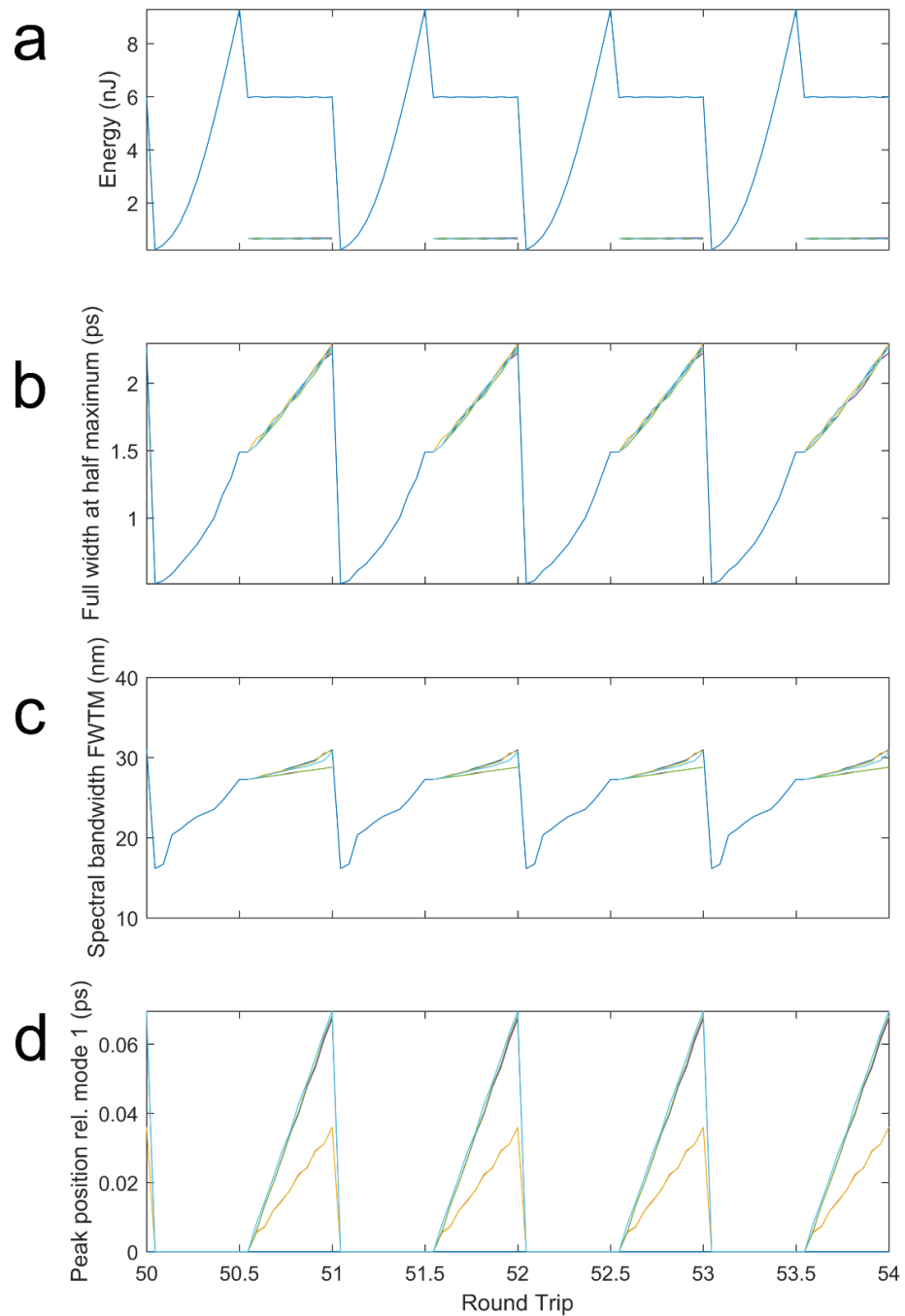


Supplementary Figure 4: Formation and evolution of a multimode mode-locked pulse in the low-energy cavity (numerical results). Evolution of the field in the low-energy cavity, corresponding to **Supplementary Figure 3**. The plots show the **a.** output pulse energy, **b.** duration, and **c.** the position of the pulse in time. After arising from noise, the mode-locked pulses' properties are stable over many round trips and do not oscillate from round trip to round trip. Due in part to its spatially-multimode nature, the mode-locked pulse moves at a finite group velocity relative to the simulation window, which moves at the velocity of the fundamental mode. The artifacts at 50, 250 and 450 round trips are due to the pulse moving from one side (-25 ps) to the other side of the simulation window (25 ps).



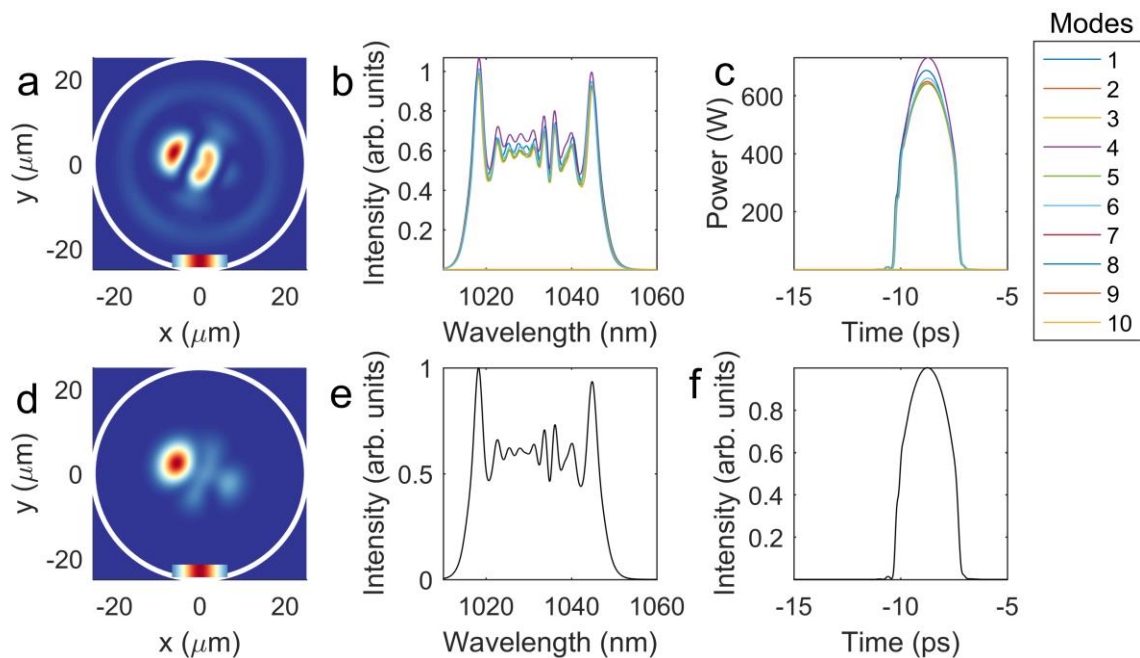
Supplementary Figure 5: intracavity pulse evolution corresponding to the previous two figures (numerical results). The figures show the evolution of **a.** the intracavity pulse energy, **b.** intracavity pulse duration, **c.** the spectral bandwidth (full width at 1/10 maximum) and **d.** the position of the pulse in each mode relative to the position of the fundamental mode pulse. The spatial and spectral filter act to restore the pulse energy, duration, bandwidth, and to undo modal dispersion, during each round trip. Different traces correspond to different modes,

for legend see **Supplementary Figure 1****Supplementary Figure 3**. Note that, since the modes fall into degenerate mode groups, several traces are overlapped in the curves shown in **d**.

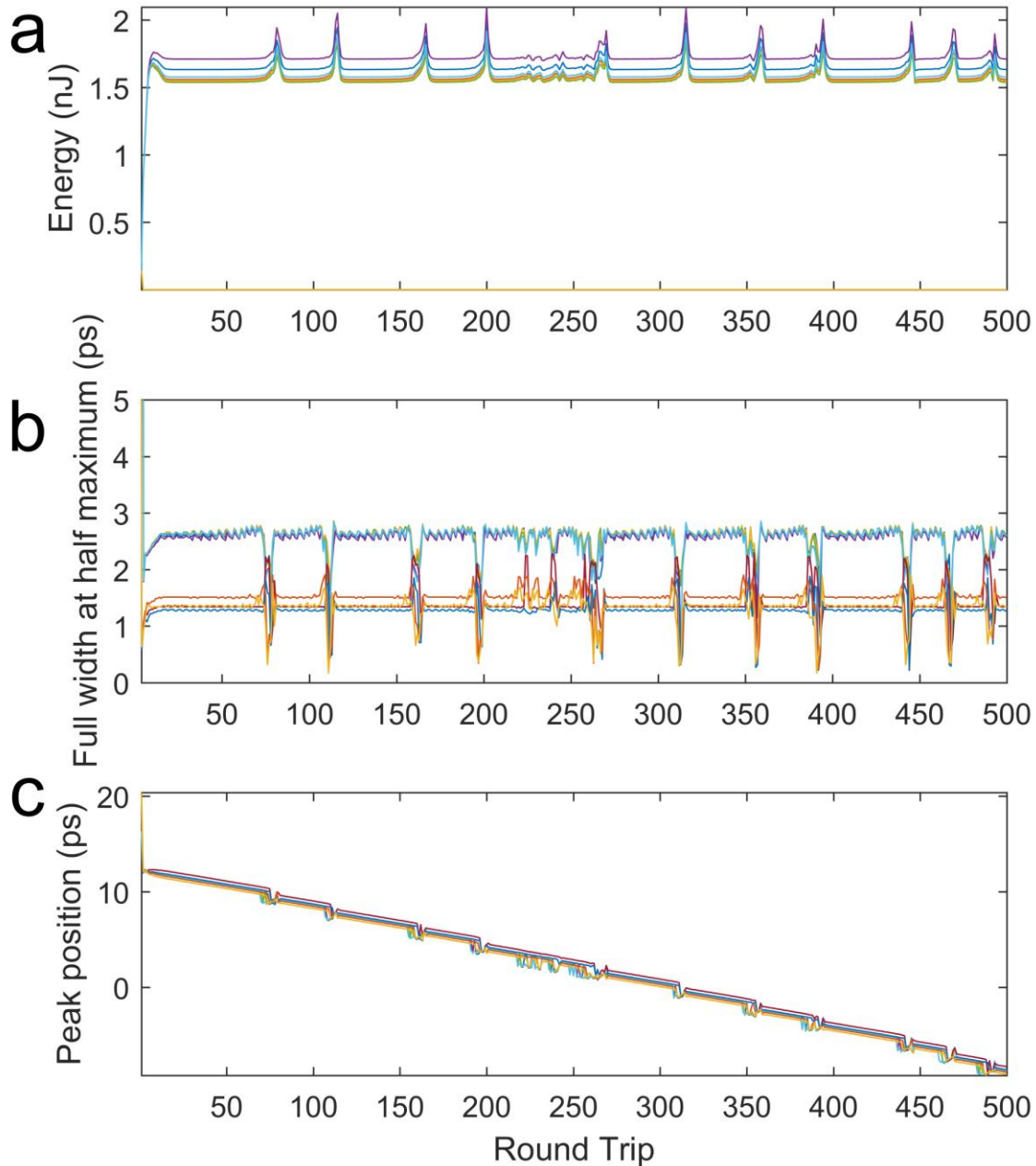


Supplementary Figure 6: steady-state intracavity pulse evolution corresponding to the previous three figures (numerical results). This figure illustrates the basic mechanism for steady-state multimode mode-locking in the low-power cavity. The pulse duration, spectral bandwidth, energy, and modal walk-off all grow monotonically in the cavity, but are reduced each round trip by the spatial and spectral filtering. The figures show the evolution of **a.** the intracavity pulse energy, **b.** intracavity pulse duration, **c.** the spectral bandwidth (full width at 1/10 maximum) and **d.** the position of the pulse in each mode relative to the position of the fundamental mode pulse. The spatial and spectral filter act to restore the pulse energy, duration, bandwidth, and to undo modal dispersion, during each

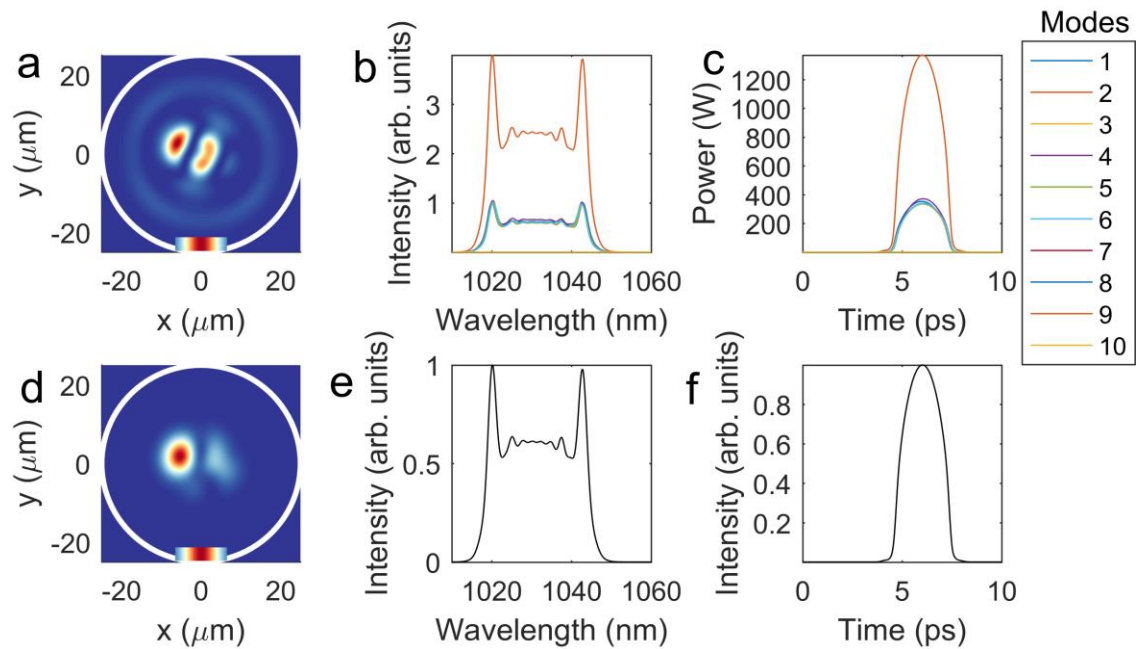
round trip. Different traces correspond to different modes, for legend see **Supplementary Figure 1** **Supplementary Figure 3**. Note that, since the modes fall into degenerate mode groups, several traces are overlapped in the curves shown in **d**.



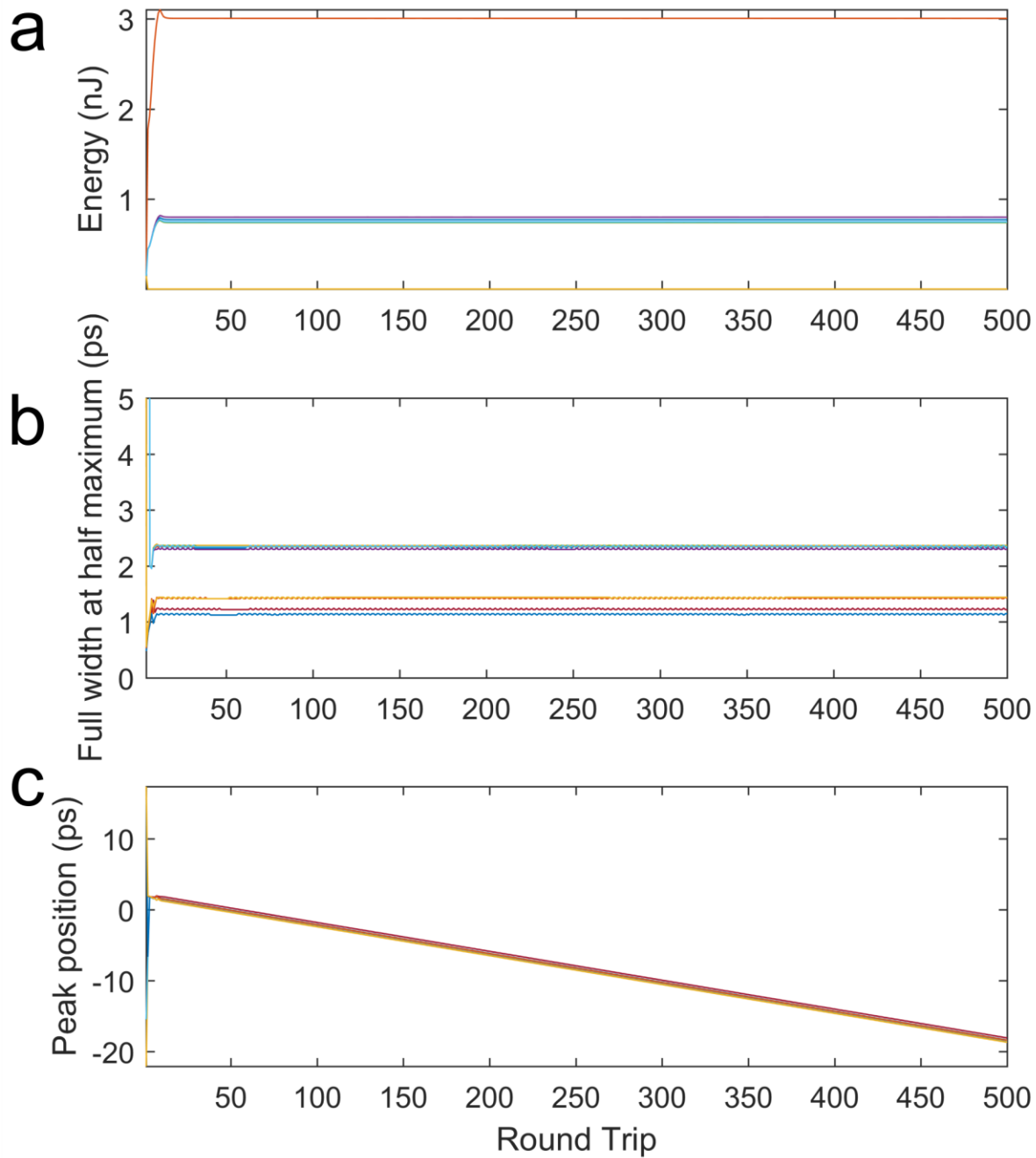
Supplementary Figure 7: Typical numerical result for the low-energy multimode cavity for multimode mode-locking with similar energy in many modes. From top left to bottom right: **a**. Initial spatial output profile, **b**. mode-resolved steady state spectra, and **c**. mode-resolved pulse intensity, **d**. steady-state output spatial profile, **e**. total steady-state spectrum and **f**. pulse intensity. The scale bars show the Gaussian intensity distribution of the fundamental mode, and the white circle indicates the fiber core. The legend in the upper right corner refers to the mode-resolved plots **b-c**. Here, the simulated modes are the first 6 lowest order modes, while modes 7-10 correspond to higher-order radially-symmetric modes which are expected to be predominantly excited. The output coupling ratio is 80%, the modulation depth is 99% (with a saturation power 4 kW), the filter bandwidth is 9 nm, the saturation energy is 3 nJ, and the passive (gain) fiber length is 50 (150) cm. The projection coefficients for passive fiber to gain fiber and from gain to passive fiber are both set to $[1 \ 1 \ 1 \ 1 \ 1 \ 1 \ 0 \ 0 \ 0 \ 0]$ (the coefficients are subsequently normalized so that their total magnitude is 1 to conserve energy at each fiber transition). The pulse is generally stable, but exhibits aperiodic collapse/death and revival.



Supplementary Figure 8: Evolution of the field for multimode mode-locking in the low energy cavity with similar energy in many spatial modes. Numerical results corresponding to **Supplementary Figure 7**. The plots show the **a.** output pulse energy, **b.** duration, and **c.** the position of the pulse in time. The mode-locked pulses' properties are stable over many round trips and do not oscillate from round trip to round trip. Due in part to its spatially-multimode nature, the mode-locked pulse moves at a finite group velocity relative to the simulation window, which moves at the velocity of the fundamental mode.

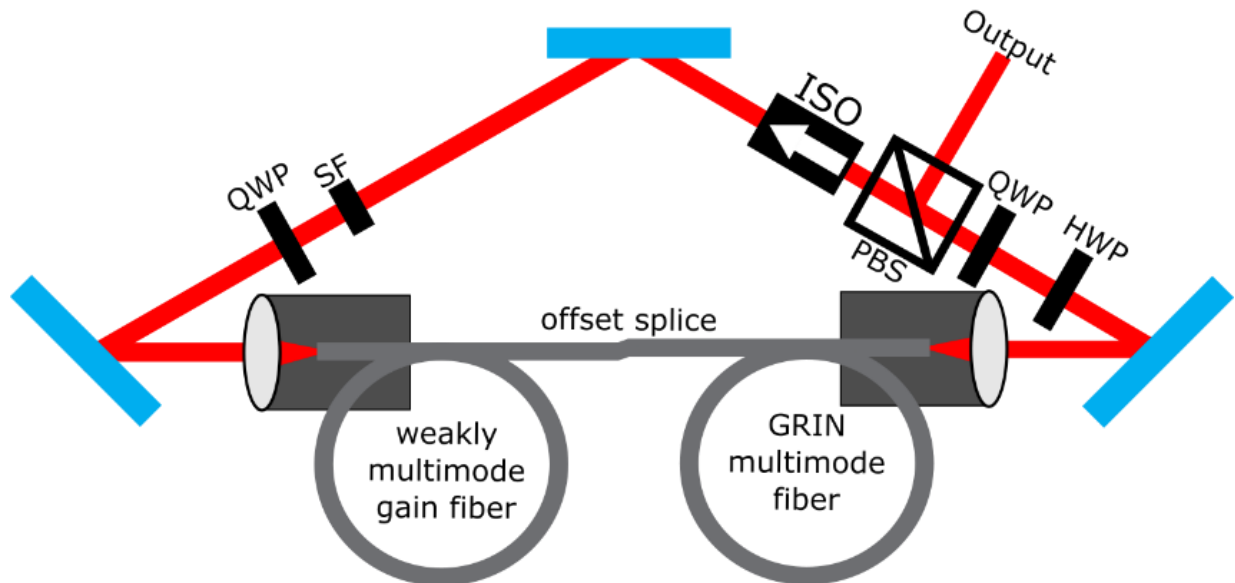


Supplementary Figure 9: typical numerical example for higher-order mode dominant multimode mode-locking in the low-energy cavity. From top left to bottom right: **a.** Initial spatial output profile, **b.** mode-resolved steady state spectra, and **c.** mode-resolved pulse intensity, **d.** steady-state output spatial profile, **e.** total steady-state spectrum and **f.** pulse intensity. The scale bars show the Gaussian intensity distribution of the fundamental mode, and the white circle indicates the fiber core. The legend in the upper right corner refers to the mode-resolved plots **b-c.** The simulated modes are the first 6 lowest order modes, while modes 7-10 correspond to higher-order radially-symmetric modes which are expected to be predominantly excited. The output coupling ratio is 80%, the modulation depth is 99% (with a saturation power 4 kW), the filter bandwidth is 9 nm, the saturation energy is 2 nJ, and the passive (gain) fiber length is 50 (150) cm. The projection coefficients for passive fiber to gain fiber and from gain to passive fiber are both set to $[1 \ 2 \ 1 \ 1 \ 1 \ 1 \ 0 \ 0 \ 0 \ 0]$ (the coefficients are subsequently normalized so that their total magnitude is 1 to conserve energy at each fiber transition).

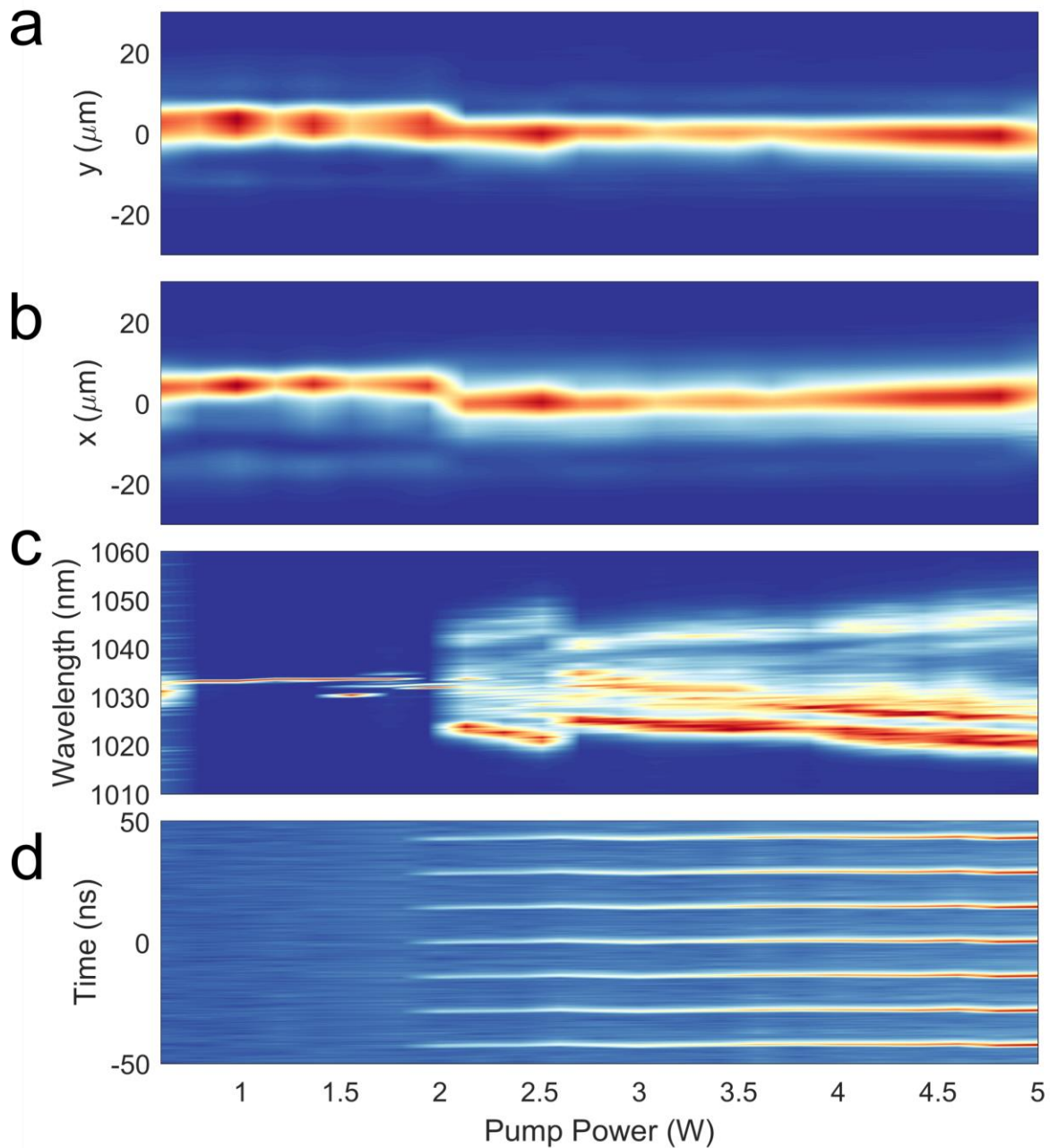


Supplementary Figure 10: Evolution of the field in low-energy cavity for higher-order mode dominant multimode mode-locking. Numerical results corresponding to **Supplementary Figure 9**. The plots show the **a.** output pulse energy, **b.** duration, and **c.** the position of the pulse in time. The mode-locked pulses' properties are stable over many round trips and do not oscillate from round trip to round trip. Due in part to its spatially-multimode nature, the mode-locked pulse moves at a finite group velocity relative to the simulation window, which moves at the velocity of the fundamental mode.

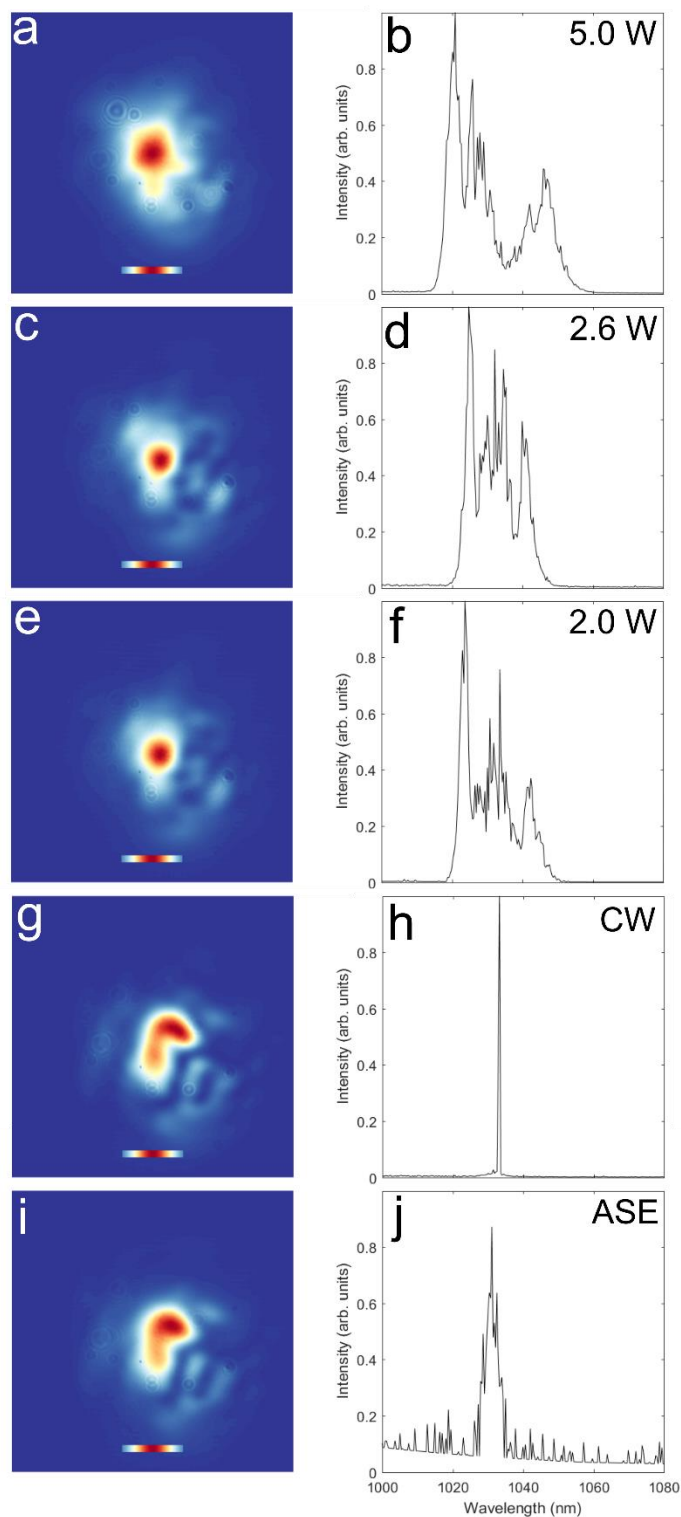
SUPPLEMENTARY EXPERIMENTAL DETAILS AND RESULTS FOR THE LOW-POWER MULTIMODE CAVITY



Supplementary Figure 11: Schematic diagram of the cavity supporting low-energy spatiotemporal mode-locking. Highly multimode excitation of the graded-index passive fiber is accomplished by a spatially-offset splice. Spatial filtering is accomplished by the overlap of the field coupled into the weakly multimode gain fiber. Nonlinear polarization rotation is used as an effective saturable absorber, controlled by the output coupling polarizing beamsplitter (PBS) and the half-wave and quarter-wave plates (HWP and QWP). The isolator ensures unidirectional light propagation in the ring cavity. An adjustable slit or pinhole provides spatial filtering, while a spectral filter (SF) is implemented using an interference filter.



Supplementary Figure 12: Measurement of spatiotemporal transition to mode-locking and spatiotemporal pulse shape evolution with pump power, in the low-energy cavity. The plots show **a-b.** cross-sections of the near-field beam profile (x, y), **c.** the spectrum, and **d.** the pulse train. The transition to mode-locking is similar to the all-multimode cavity, but we are able to access interesting regimes above the mode-locking threshold. As the pump power is changed above the threshold, we observe changes in the beam profile and spectrum. As the pulse energy grows, the spectrum goes through a period of broadening (2-2.5 W), then suddenly shrinks. At this point the beam profile exhibits some subtle changes indicating a change in the modal composition of the pulse. Higher pump powers cause slow spectral broadening and spatial changes in the beam. Given the spatiotemporal nature of the pulse – its modal composition varies with wavelength and time – estimation of the mode composition is difficult. However, a reasonable hypothesis is that the fundamental mode energy grows monotonically from ~ 2.5 to 5 W.



Supplementary Figure 13: Near-field beam profiles and spectra corresponding to the indicated points in the previous Supplementary Figure. The plots show the measured beam profile and spectrum for the ASE (i, j), the CW lasing state (g, h), the first mode-locked state at 2 W pump power (e, f), the changed mode-locked state at 2.6 W

(c, d), and the highest-power state shown at 5 W (a, b). The scale bar is the Gaussian intensity of the 13 μm mode field diameter fundamental mode.

SUPPLEMENTARY SIMULATION DETAILS AND RESULTS FOR THE ALL-MULTIMODE CAVITY

As described in the methods, we use a (2+1)-D GNLS to provide a qualitative model for spatiotemporal mode-locking in a MM fiber based cavity.

$$\begin{aligned} \partial_z A(x, z, t) = & \frac{i}{2k_o(\omega_o)} \partial_{xx} A + i \frac{k_o(\omega_o)}{2} (n(x)^2 - 1) A \\ & + \sum_{m=2}^3 i^{m+1} \frac{\beta_m}{m!} \partial_t^m A + A \frac{g_o(\omega)}{1 + \frac{\int |A(x, z, t')|^2 dt'}{I_{gs}}} \\ & + i\gamma \left(1 + \frac{i}{\omega_o} \partial_t\right) [(1 - f_R) |A|^2 A + f_R \int_{-\infty}^t d\tau h_R(\tau) |A(x, z, t - \tau)|^2] \end{aligned}$$

where $k_o(\omega_o)$ is the propagation constant at the center angular frequency ω_o , $n(x)$ is the index profile, β_m are the m^{th} order chromatic dispersion terms, $g_o(\omega)$ is the small-signal gain spectrum, $\gamma = n_2 k_o$ is the nonlinear coefficient, f_R is the Raman fraction and $h_R(\tau)$ is the Raman response of the medium. The diffraction, dispersion and gain terms are numerically implemented in the frequency domain. To improve calculation speed, except where noted otherwise, $f_R = 0$ and the shock term proportional to $\frac{i}{\omega_o} \partial_t$ is neglected.

Full accounting of gain saturation (*i.e.*, not using a Taylor expansion for the 4th term above) is expected to be important for stable solutions and a full spatiotemporal saturable absorber, *i.e.*

$$A(x, z, t) \rightarrow A(x, z, t) \sqrt{1 - \frac{\text{mod_depth}}{1 + \frac{|A(x, z, t)|^2}{I_{sat}}}}$$

is expected to play an important role in stable spatiotemporal mode-locking. These effects cannot be easily incorporated into a set of coupled mode equations such as the GMMNLSE and furthermore, it is of interest whether pulses are stable in the presence of all guided modes, rather than merely a subset. Therefore, full-field spatiotemporal simulations are important to supplement the coupled-mode model described previously. However, given that many round trips constitute roughly 10^3 m of propagation and the required longitudinal step size is roughly 10^{-5} m, to conduct simulations in a reasonable timeframe we chose to simplify the physics by neglecting one of the spatial dimensions. A similar approach has proven to have surprising qualitative and even quantitative accuracy in studies of solitons in graded-index waveguides [1, 3-5]. Future work will explore more rigorous 3D models of spatiotemporal mode-locking.

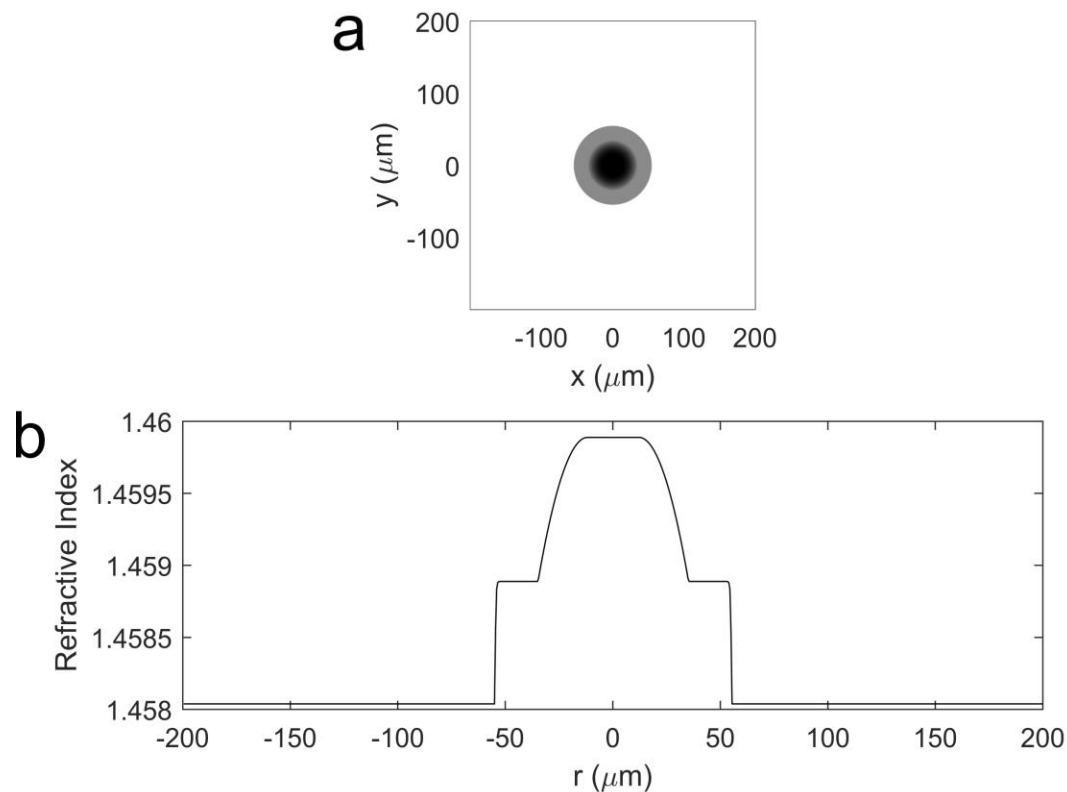
Supplementary Figure 14 shows the ideal index profile for the fiber used in experiments, while the one-dimensional profile was used for the simulations.

Supplementary Figure 15 shows the steady-state intracavity pulse evolution corresponding to the maximum gain saturation energy of the sequence shown in **Figure 3**.

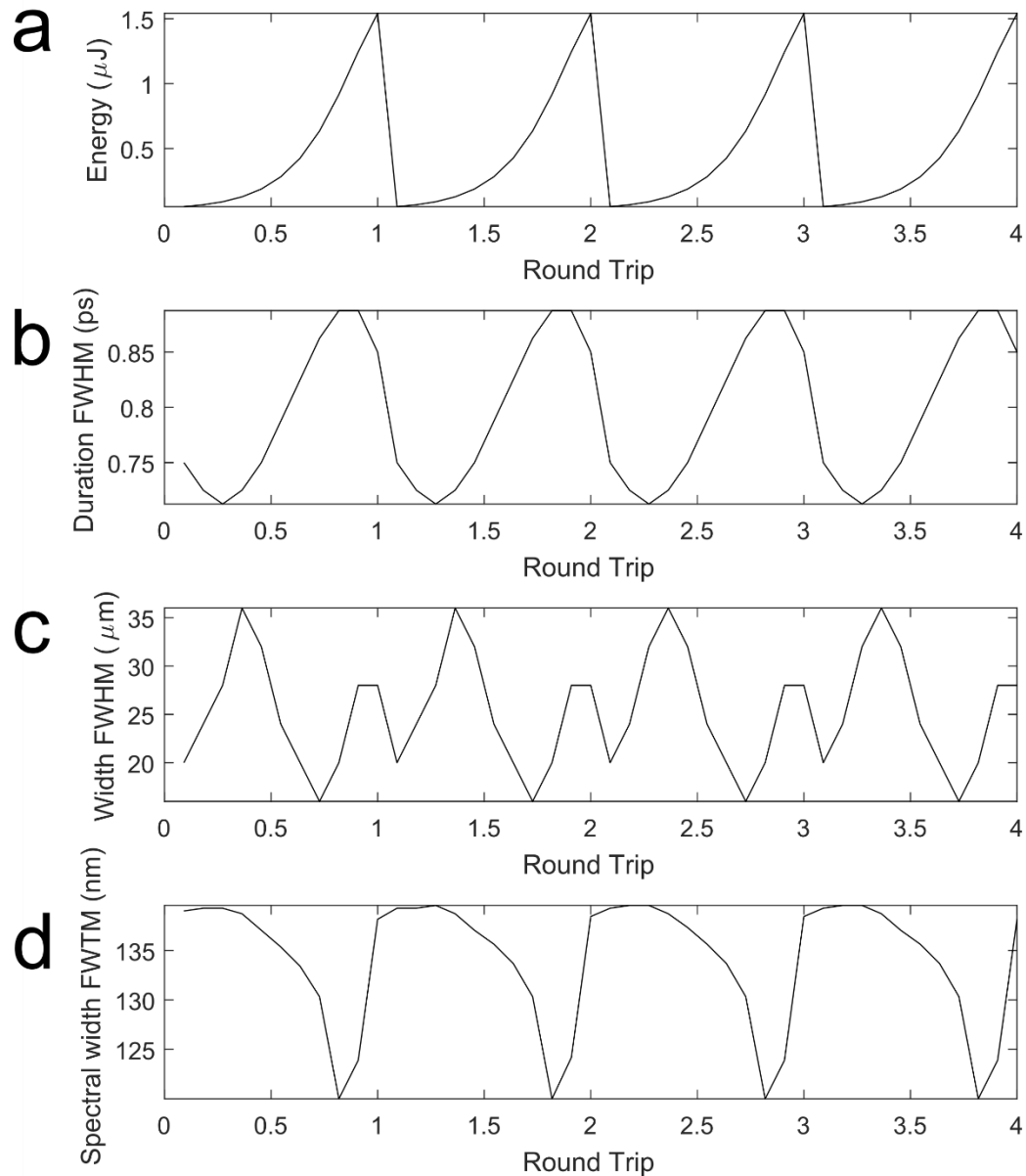
Supplementary Figure 16 and **Supplementary Figure 17** show the effect of forcing highly spatially multimode mode-locking to occur by reducing the filter dimensions below the fundamental mode size.

Supplementary Figure 18 and **Supplementary Figure 19** show noise-like pulsations and dark soliton formation in the all-multimode fiber cavity simulations.

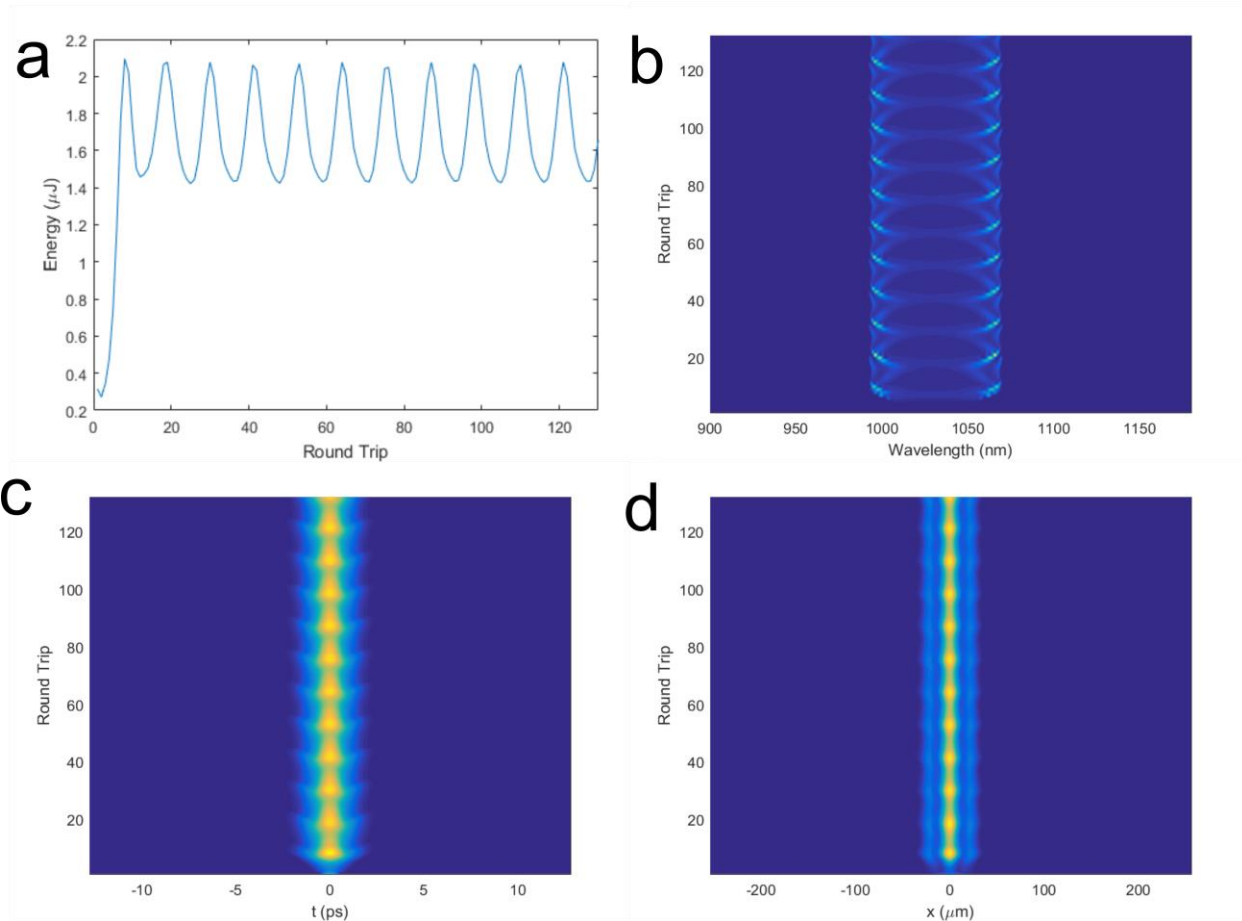
Supplementary Figure 20 and **Supplementary Figure 21** show numerical predictions of high-power Gaussian pulse formation in a cavity using a fiber double the size of the one used in our experiments and prior simulations.



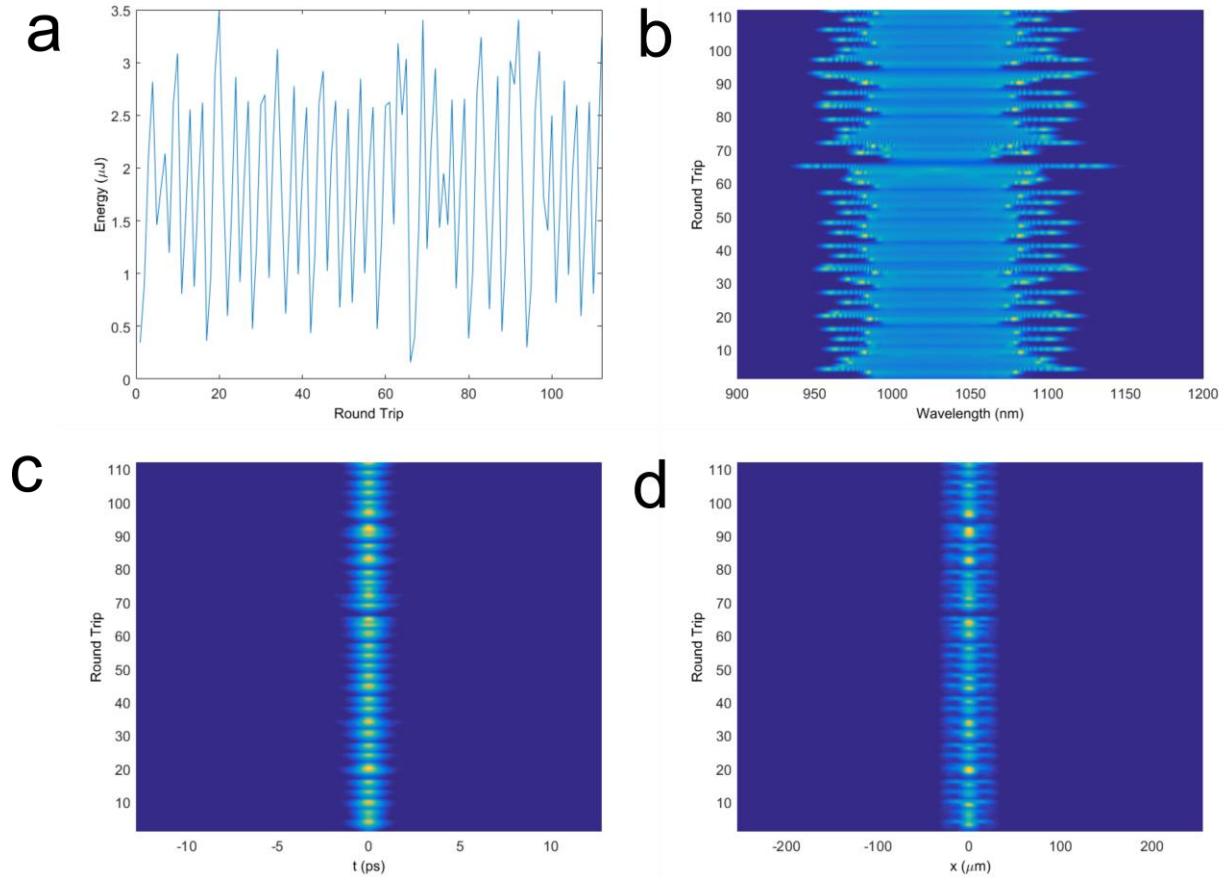
Supplementary Figure 14: Index profile of the partially-graded multimode Yb-doped fiber used for the all-multimode fiber cavity. a. The 2D, radially-symmetric nominal profile of the fiber used in the experiments, **b.** a cross-section of **a**, and the 1D index profile used in the (2+1)D simulations.



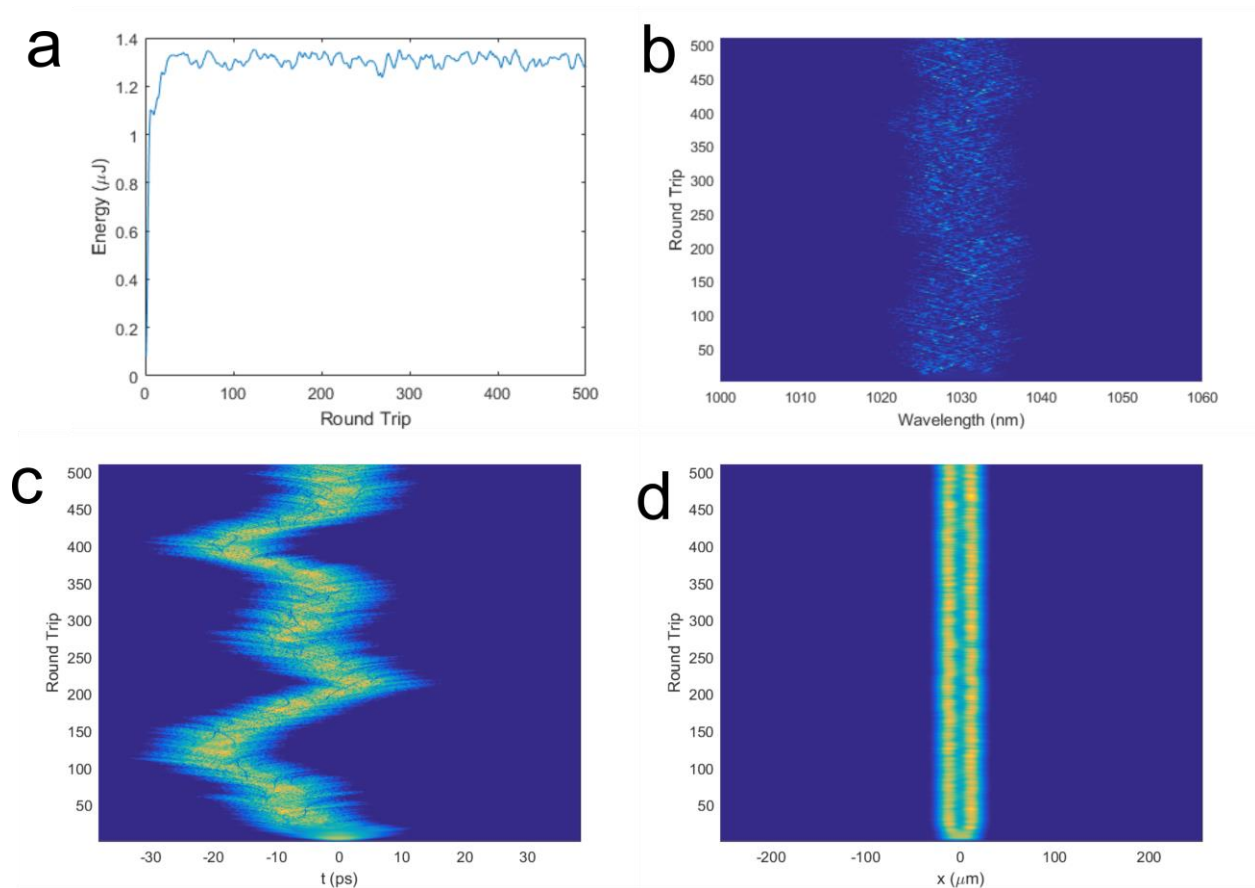
Supplementary Figure 15: Steady-state intracavity pulse evolution corresponding to the highest-energy condition shown in Figure 3. The maximum gain saturation for the sequence shown in Figure 3 is held constant. The figures show the evolution of **a.** the intracavity pulse energy, **b.** the intracavity pulse duration, full width at half maximum, **c.** the spatial width, and **d.** the spectral bandwidth, full width at 1/10 maximum. All parameters of the pulse exhibit a periodic evolution, and the spatial breathing shows evidence for the spatially-multimode nature of the pulse. The evolution continues indefinitely, but only the first 4 round trips are shown for clarity. These plots illustrate that, similar to the low-power cavity, for which intracavity evolution is plotted in **Supplementary Figure 5-6**, the spatiotemporally mode-locked pulse breathes in energy, duration, spatial dimensions and spectral bandwidth. All these quantities are periodically reduced by spectral and spatial filtering (and for the energy, output coupling and linear losses). Importantly, the strong spatial breathing shown in **c.** illustrates that, despite the stable Gaussian output profile of the pulse, the field within the cavity is multimode.



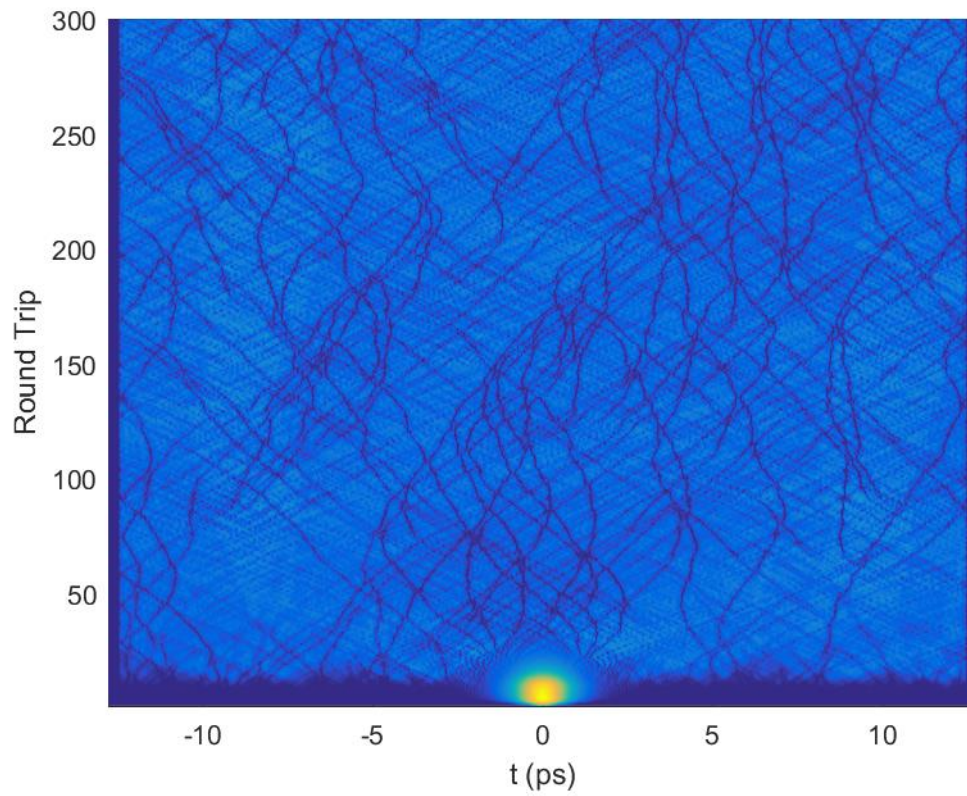
Supplementary Figure 16: Numerical results in the high-power cavity showing periodic oscillations of a spatiotemporally-mode-locked pulse for spatial filtering below the fundamental mode size. From top left to bottom right, the plots show **a.** the output energy, **b.** spectrum, **c.** time and **d.** spatial profile. All evolve with a period of ~ 10 round trips. This behavior is observed for a spatial filter roughly $\frac{1}{4}$ the fundamental mode size.



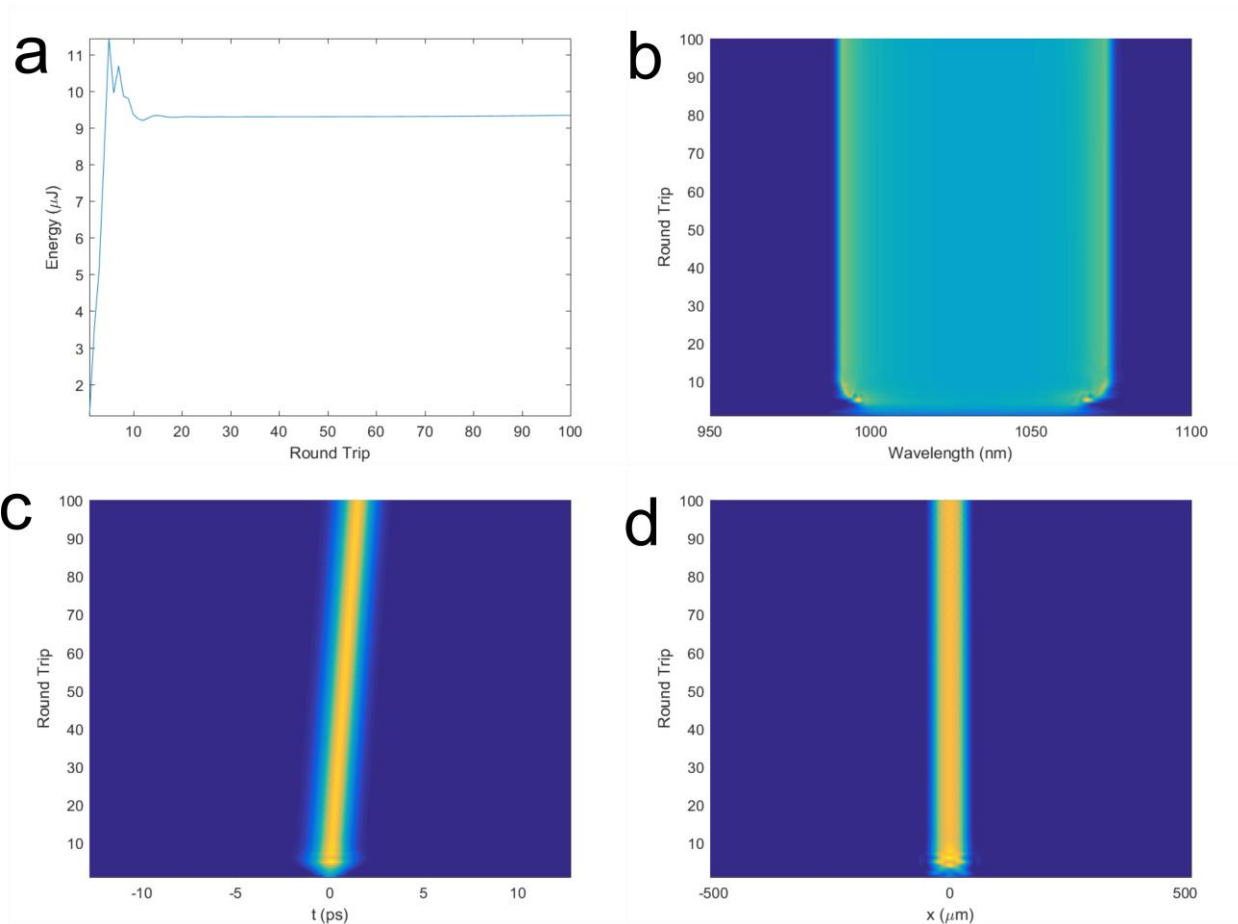
Supplementary Figure 17: Numerical simulation of aperiodic evolution of a spatiotemporally-mode-locked pulse in the high-power cavity for strongly sub-fundamental spatial filtering. From top left to bottom right, the plots show **a.** the output energy, **b.** spectrum, **c.** time and **d.** spatial profile. Chaotic pulsations without noise-like pulsing. The observed behavior occurs for spatial filters $<1/8$ the fundamental mode size. Transform-limited peak powers near 0.25 GW occur despite the relatively small average mode-field diameter.



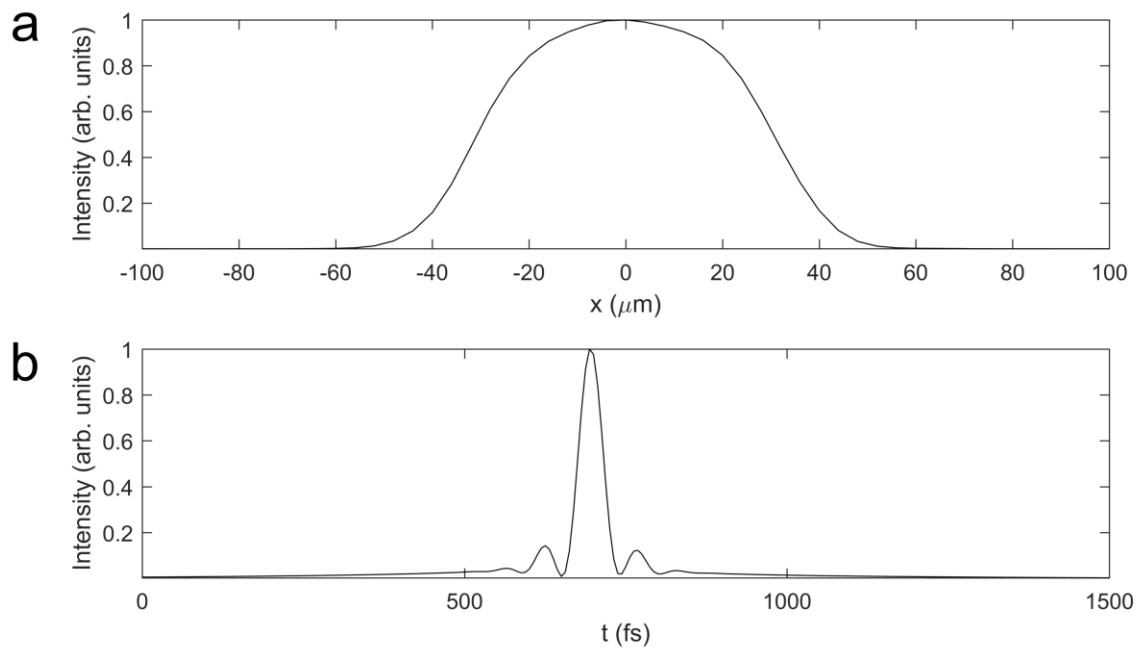
Supplementary Figure 18: Example numerical result in the high-power cavity showing noise-like multimode pulse formation. From top left to bottom right, the plots show **a.** the output energy, **b.** spectrum, **c.** time and **d.** spatial profile. The energy is roughly stable, but the pulse exhibits a random-walk behavior that results from the complex changing mixture of modes that make it up. Dark pulse traces can be seen in the pulse over multiple round trips.



Supplementary Figure 19: Example of numerical simulation showing multimode dark soliton formation. The other aspects of the evolution are similar to the previous figure.

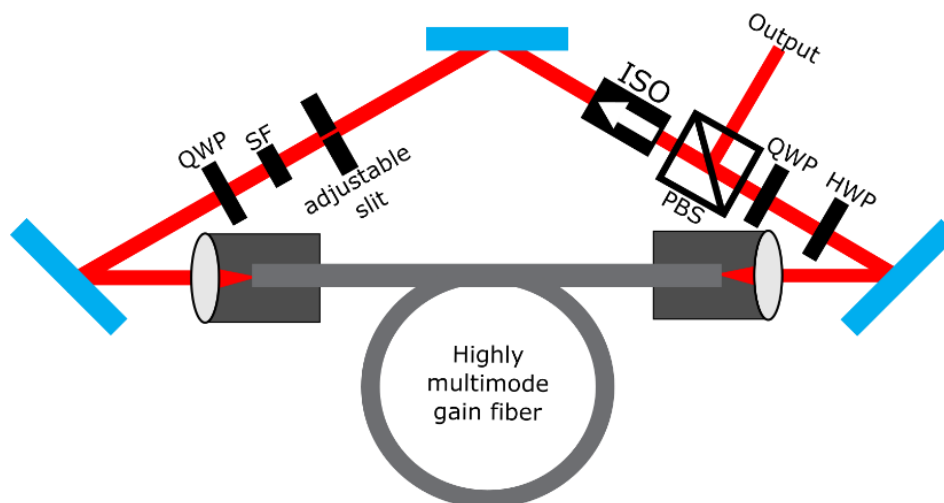


Supplementary Figure 20: Numerical simulation of mode-locked pulse formation in a larger fiber multimode fiber cavity. From top left to bottom right, the plots show **a.** the output energy, **b.** spectrum, **c.** time and **d.** spatial profile. To investigate scaling to higher performance, we consider a fiber twice the size (but similar numerical aperture and profile) as the one shown in Supplementary Figure 14. Here we include stimulated Raman scattering and self-steepening in the model, since these higher-order effects are expected to become important for limiting performance levels. The results show stable, nearly 10 μJ pulses can form. These pulses have a nearly Gaussian spatial profile, are nearly identical from round-trip to round-trip, and have a slightly shifted group velocity.

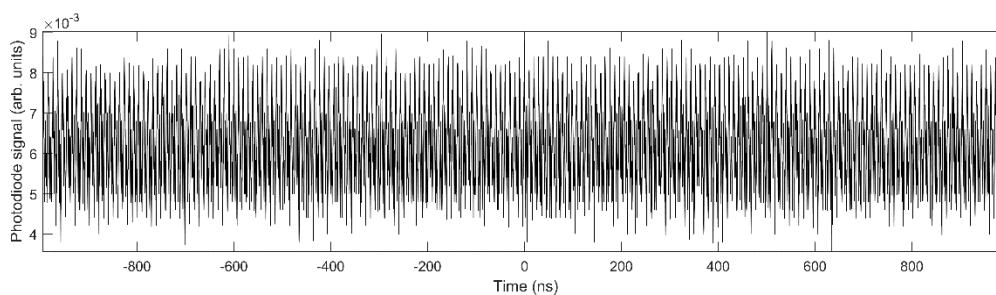


Supplementary Figure 21: High energy pulse in numerical simulation of larger high-power multimode cavity. a. The stable spatial profile and **b.** the dechirped pulse temporal profile corresponding to the previous figure. The resulting peak power is roughly 0.2 GW.

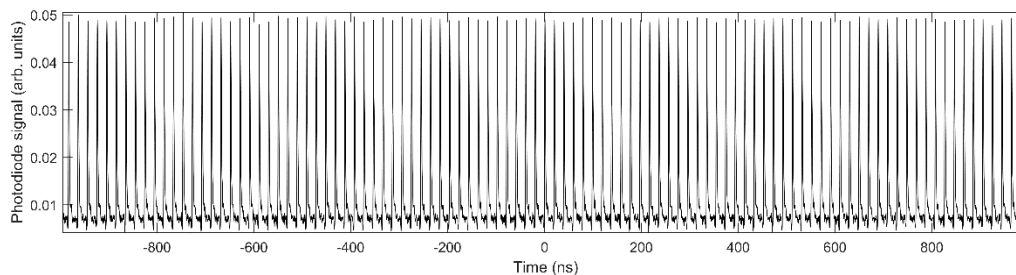
SUPPLEMENTARY EXPERIMENTAL DETAILS AND RESULTS FOR THE ALL-MULTIMODE CAVITY



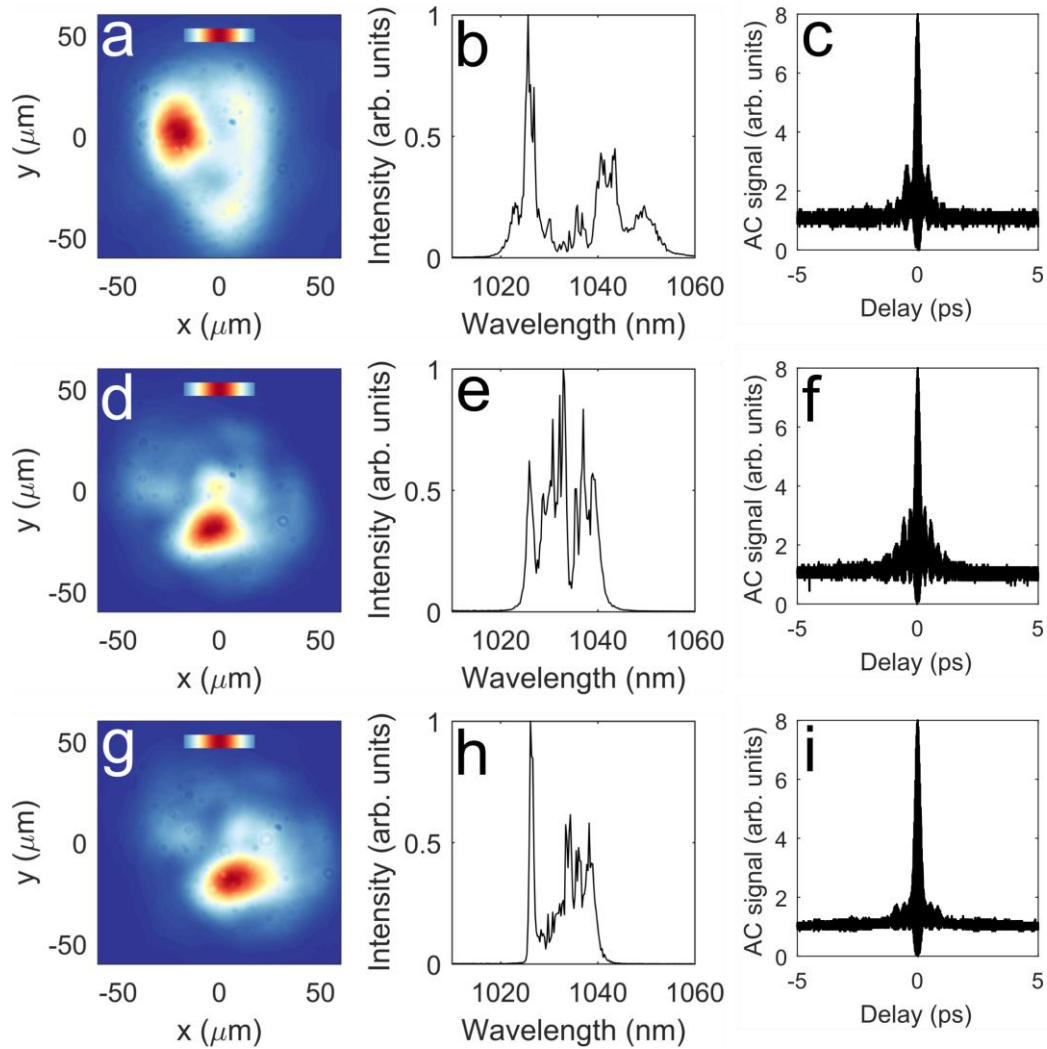
Supplementary Figure 22: Schematic diagram of the all-multimode fiber cavity. Nonlinear polarization rotation is used as an effective saturable absorber, controlled by the output coupling polarizing beamsplitter (PBS) and the half-wave and quarter-wave plates (HWP and QWP). The isolator ensures unidirectional light propagation in the ring cavity. An adjustable slit or pinhole provides spatial filtering, while a spectral filter (SF) is implemented using an interference filter.



Supplementary Figure 23: Fast photodetector measurement corresponding to pump power 18 W in Figure 4b.



Supplementary Figure 24: Fast photodetector measurement corresponding to pump power 30 W in Figure 4b.



Supplementary Figure 25: Examples of multimode mode-locked state observed experimentally. a-c, d-f, and g-i show the near-field beam profile, spectrum, and dechirped autocorrelation for different mode-locked states observed in the same cavity for different waveplate positions and mirror alignments. For a-c, the pulse energy is 100 nJ, the transform limited duration is 100 fs and the measured pulse width is 140 fs assuming a 1.4 deconvolution factor. For d-f, the pulse energy is 82 nJ, and the transform limited and measured durations are both 170 fs. For g-i, the pulse energy is 130 nJ and the transform limited and measured pulse durations are both 190 fs. The scale bar in a,d,g shows the Gaussian profile of the fundamental mode of the fiber.

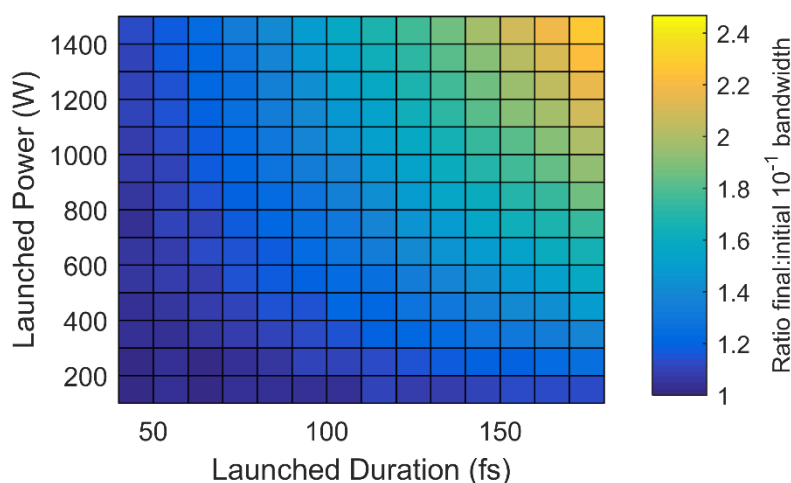
PEAK POWER ASSESSMENT

Assessing the peak power of the generated pulses is important in order to rule out large contributions from a continuous-wave (CW) background (which can sometimes be indicated in the spectrum) or multi-pulsing. In combination with the many other measurements taken of the output field, this helps to confirm the stable spatiotemporal mode-locking we observe. However, measuring the peak power of even standard single mode fiber oscillators is non-trivial. We use two approximate checks that confirm that the peak power is within a factor of 2 or so of the expected value assuming single pulsing without strong CW background.

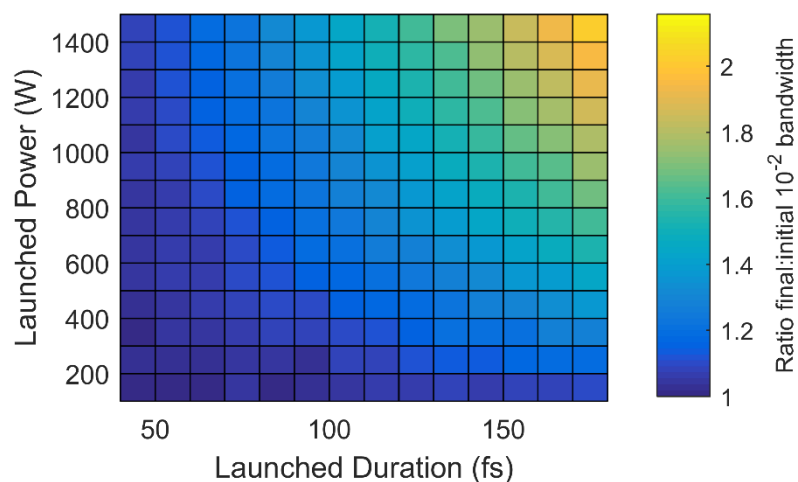
Approach 1: spectral broadening in single-mode fiber

A common approach is to launch sampled portions of the pulse train into single-mode fiber and compare the measured spectral broadening from self-phase modulation with numerical simulations. For the pulses in the multimode fiber lasers, we observe different spectra depending on how the light is coupled into the single-mode fiber, reflecting the spatiotemporally-complex nature of the pulse. However, because other measurements which average over the entirety or most of the field (spectrum, pulse train, interferometric autocorrelation, RF spectrum) imply that these variations are small over the pulse, we expect this approach is still valuable as a rough estimate or “sanity check.”

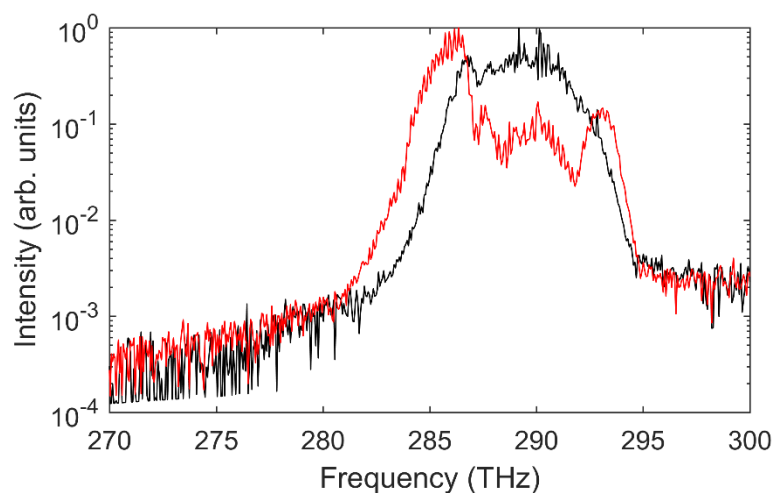
Supplementary Figure 26 and **Supplementary Figure 27** show the results of simulations using the GNLSE, starting with transform-limited Gaussian pulses with an initial noise level 10 times the shot noise level.



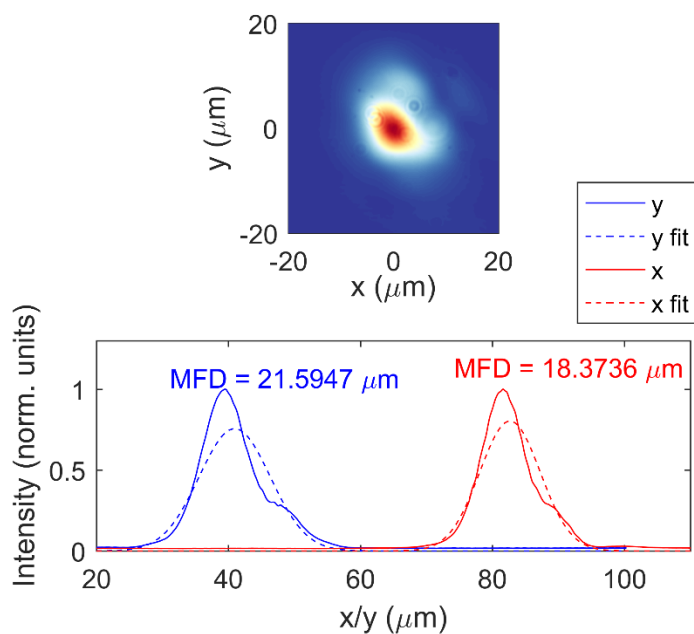
Supplementary Figure 26: The ratio of final to initial spectral bandwidth at 0.1 times the maximum, as a function of the pulses’ initial peak power and duration, after propagation through 5 m of fiber in simulation.



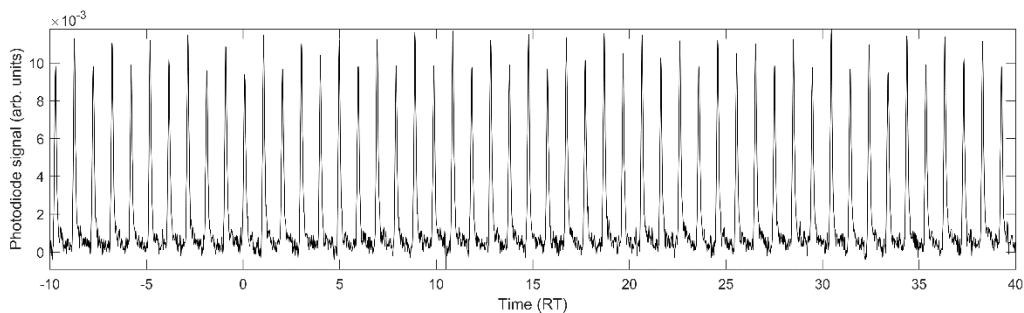
Supplementary Figure 27: The ratio of final to initial spectral bandwidth at 0.01 times the maximum, as a function of the pulses' initial peak power and duration, after propagation through 5 m of fiber in simulation.



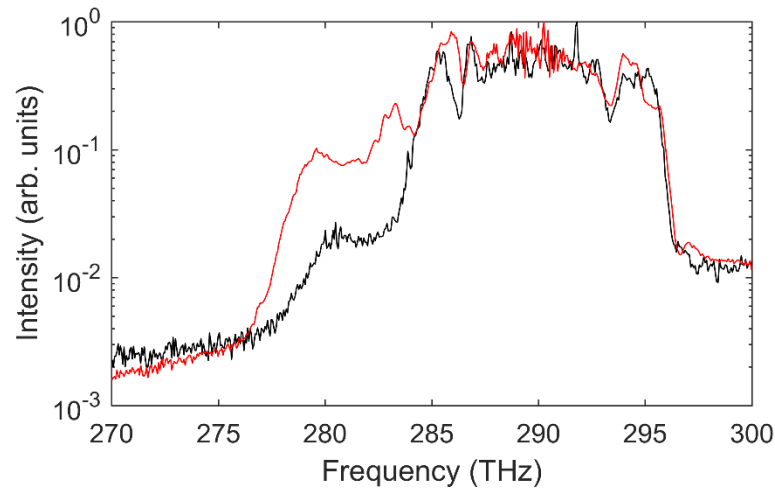
Supplementary Figure 28: Assessment of peak power, example 1. The red curve shows the spectrum after 5-m of HI1060 fiber, for a coupled power of 4 mW. The black shows the spectrum measured using a long 400 μm diameter multimode fiber. In 5-m of HI1060 fiber, the spectral width at 10⁻¹ (10⁻²) broadens by a factor of 43% (20%) compared to the oscillator output spectrum. Comparison with the numerically-calculated spectral broadening for transform-limited Gaussian pulses in the same fiber (**Supplementary Figures 23-24**) implies a peak power of ~0.4-1.0 kW (uncertainty here stems from the uncertain initial pulse duration). For the condition shown, the oscillator's repetition rate is 62.5 MHz and the output power is 2.0 W (pulse energy 32 nJ). The beam profile is multimode and the pulse train exhibits multi-round trip periodicity, shown below. The coupled sample of 4 mW corresponds to 64 pJ, which for the ~100 fs duration implies ~0.6 kW peak power.



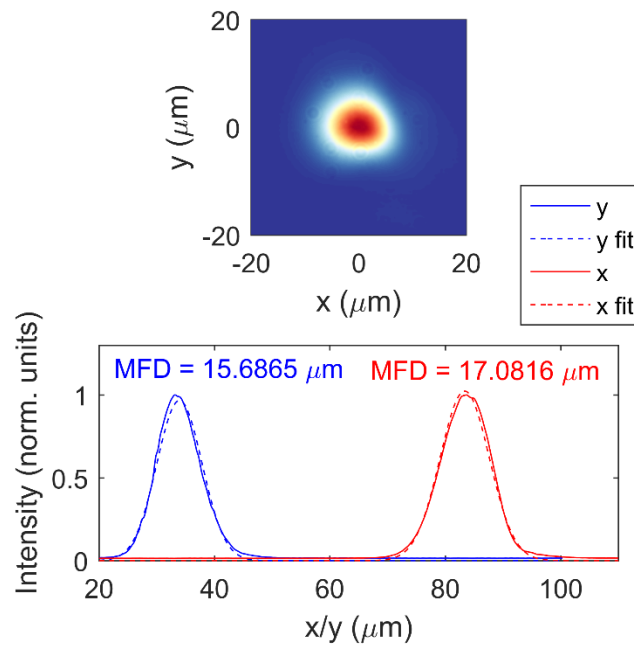
Supplementary Figure 29: near-field beam profile for the mode-locked state considered in previous figure. Top: near-field beam profile, bottom: Gaussian fit to cuts through maximum intensity.



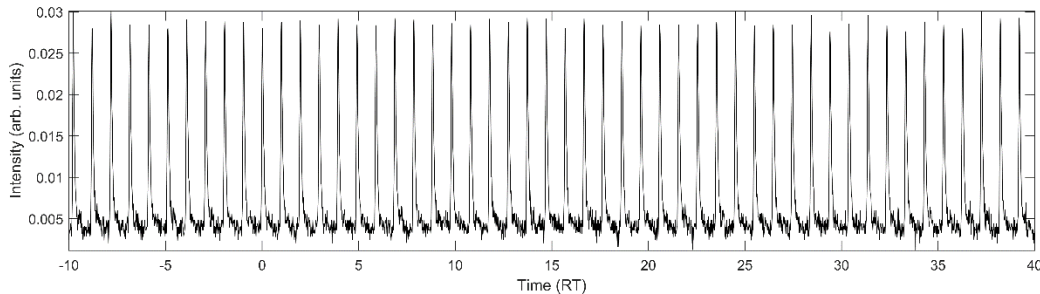
Supplementary Figure 30: Pulse train measurement for mode-locked state considered in previous figure. RT is the cavity round trip time. The pulse train exhibits oscillations over multiple round trips, which is a common but not typical feature of the multimode mode-locked states we observe.



Supplementary Figure 31: Assessment of peak power, example 2. For 5 mW coupled into 5-m of HI1060 fiber, the spectral width at 10^{-1} (10^{-2}) broadens by a factor of 33% (20%) compared to the measured spectrum in the large MMF. These correspond to ~ 0.6 to 1.0 kW peak power by comparison with **Supplementary Figure 23-24**.



Supplementary Figure 32: Near-field beam profile corresponding to the mode-locked state considered in the previous figure. The beam is larger than the fundamental mode by $>20\%$, but is evidently dominated by the fundamental mode.



Supplementary Figure 33: Pulse train measurement corresponding to the mode-locked state considered in previous figure.

Approach 2: analytic estimate of intracavity nonlinear phase shift

In addition, since the spectral breathing ratio of the pulse evolution is known (the ratio of the output bandwidth to the bandwidth of the spectral filter), a second check can be made by comparing the *expected* peak nonlinear phase shift of the pulse, assuming formation of either dissipative solitons or similariton pulses, with the value calculated assuming the output pulse energy corresponds to a single, background-free pulse, and knowing the fiber length, the output mode area and the estimated gain and loss of the cavity.

For ~ 40 - 50 MHz dissipative soliton fiber cavities, the correlation of nonlinear phase shift with spectral breathing ratio is well-established [6], and meanwhile for similaritons the peak nonlinear phase shift accumulated in the gain fiber can be shown analytically to be:

$$\varphi_{NL} = \frac{3\gamma}{8} \left(\frac{gU_{in}}{\sqrt{\beta_2\gamma/2}} \right)^{2/3} \left(\frac{\omega_p}{\omega_o} \right)^2$$

The additional nonlinear phase in other fibers of length L can be estimated as $\frac{L}{L_{nl}}$, where $L_{nl} = \frac{A_{eff}}{k_o n_2 P}$, where P is the peak power of the chirped pulse, A_{eff} is the effective mode area, k_o is the vacuum wavenumber and n_2 is the nonlinear index. We assume weak spatial breathing (the output mode-field diameter is roughly the same through the cavity), output coupling in the typical range of 30-70%, and take into account the 9 nm filter bandwidth and typical measured chirped duration and spectral bandwidth of the output pulse.

As an example, we consider the mode-locked state at 30 W pump power in Figure 4. Similar analysis can be carried out for all the other mode-locked states we observe, which yield quite similar conclusions. The output spectrum combined with the 9-nm filter corresponds to a spectral breathing ratio of ~ 1.5 - 2 . The spectrum and breathing are most consistent with dissipative soliton pulse shaping, so we expect by comparison with [6] that if the laser is single-pulsing, and the output field consists only of the mode-locked pulse, the nonlinear phase shift is 3 - 4π .

To assess, we assume the measured average power divided by the repetition rate of the measured pulse train gives the energy in the single pulse. From this, we estimate the nonlinear phase shift to confirm whether it is consistent with, or contradicts, the expected value above. A Gaussian fit of the output beam profile gives an effective mode area (A_{eff}) of $3850 \mu\text{m}^2$ and the output pulse duration is ~ 1.5 ps. The average intracavity pulse energy is taken to be $E_{in,eff} = \frac{E_{out}}{OC} f$, where $f = \frac{1}{LE_{final}} \int_0^L E(z) dz$ and E is the pulse energy and E_{final} is the energy before output coupling. Taking the cavity-averaged peak power to be $P = \alpha E_{in,eff} / T_{out}$, where α is a constant factor near 0.94 for a Gaussian pulse, the nonlinear phase shift is $\frac{L}{L_{nl}}$, where $L_{nl} = \frac{A_{eff}}{k_0 n_2 P}$ and L is the fiber length in the cavity. From this, we can write that $\varphi_{NL} = \frac{L k_0 n_2 \alpha f E_{out}}{A_{eff} T_{out} OC}$. For the 3.6 m long fiber in the cavity, and taking $n_2 = 2.3 \cdot 10^{-20} \text{m}^2/\text{W}$, we obtain $\varphi_{NL} \approx 11.4 \alpha f / OC$.

Reasonable estimates for f are in the range 0.3-0.8, which is the same as the expected values of OC (however, if OC is higher, f is expected to be lower). Taking 0.3 and 0.8 as the min/max values for OC and f , and $\alpha = 0.94$, the estimated nonlinear phase shift is $\varphi_{NL} \approx (5 \pm 2)\pi$, which is consistent with the expected $3-4\pi$ value. It is interesting that this shift exceeds the expected value for single-mode dissipative solitons, which would be expected for MM dissipative solitons. However, both methods described here provide confirmation of the peak power to within a factor of 2 or so, so the apparent quantitative agreement should not be taken as significant.

DISCUSSION OF SPATIOTEMPORAL DISPERSION/COUPLING IN SPATIOTEMPORALLY MODE-LOCKED PULSES

In this section we examine numerically the spatiotemporal properties – the dispersion or space-time coupling – present in spatiotemporally mode-locked pulses. For the majority of situations we consider in this work, these effects are small. However, these represent an important distinction from conventional mode-locked pulses, which may be important for future developments.

For normal dispersion mode-locking in single-mode fiber, dissipative solitons and similaritons in general have a substantial chirp. For single-mode lasers, this can be removed by a diffraction grating compressor to produce nearly transform-limited pulses. For the multimode pulses formed here, we expect not only a chirp in time, but also a spatiotemporal pulse structure due to spatial, or modal, dispersion.

Consideration of spatiotemporal pulse dispersion is not, however, novel for spatiotemporally mode-locked pulses. All dispersive, spatially inhomogeneous optical components (e.g., diffraction grating compressors, lenses, etc.) introduce significant spatiotemporal coupling, or

spatiotemporal dispersion. For example, focusing by a lens – which is a spatially inhomogeneous dispersive element – leads to a focus in which a conventional mode-locked pulse is, without prior compensation, spread out in spacetime over 100-1000 fs. An excellent overview is provided in [7] and its references. This has been the main driver for the development of spatiotemporal pulse measurement tools historically, and consideration of spatiotemporal coupling is necessary for use of ultrashort pulses in general.

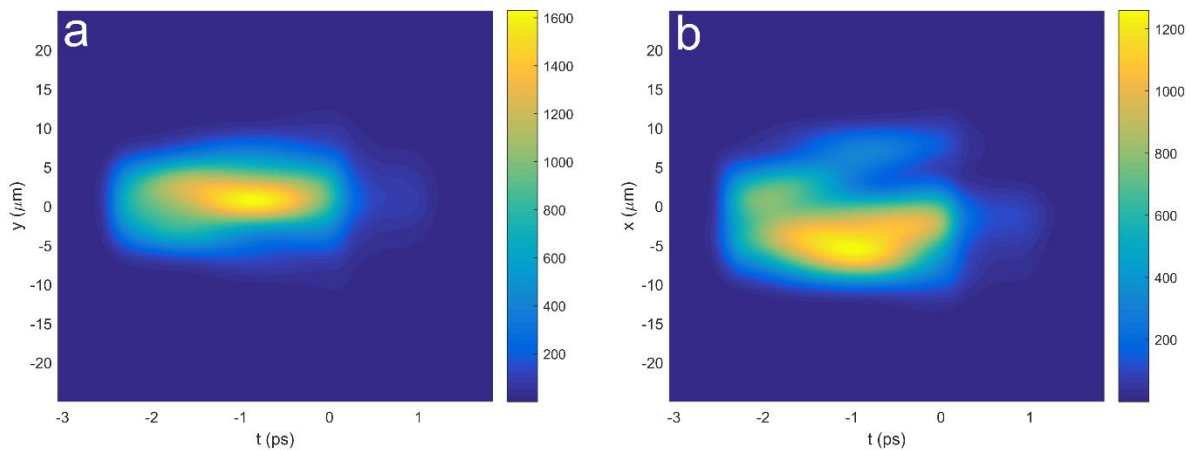
Most spatiotemporally mode-locked states we observe, in simulation and experiment both, exhibit only small spatiotemporal dispersion, and in the context of conventional applications we expect this to be of no greater importance than for conventional mode-locked oscillators. While spatiotemporal dispersion means that certain multimode mode-locked states cannot be compressed to their transform limit using simple optical techniques, we find that it is easy in both experiments and simulations to obtain a variety of multimode mode-locked states with small modal dispersion (corresponding to round-trip walk-off smaller than the transform-limited pulse duration). Remarkably, this is even true when the continuous wave state comprises ~ 100 spatial modes. This observation may be related to the condensation-like nonlinear attraction to low-order modes that has now been observed in many works studying multimode GRIN fibers [8-12]. This is confirmed by the results below, and experimentally by the nearly transform-limited autocorrelations and peak-power.

Supplementary Figures 34-36 show the spatiotemporal dispersion properties for a mode-locked pulse (also shown in **Supplementary Figures 3-6**) which is similar in spatial mode content to typically-observed spatiotemporally-mode-locked pulses such as those presented in Figure 2. These examples show that, for most spatiotemporally mode-locked pulses, spatiotemporal dispersion compensation can improve the pulse quality, but has an overall small effect. This explains why we can observe nearly transform-limited autocorrelations.

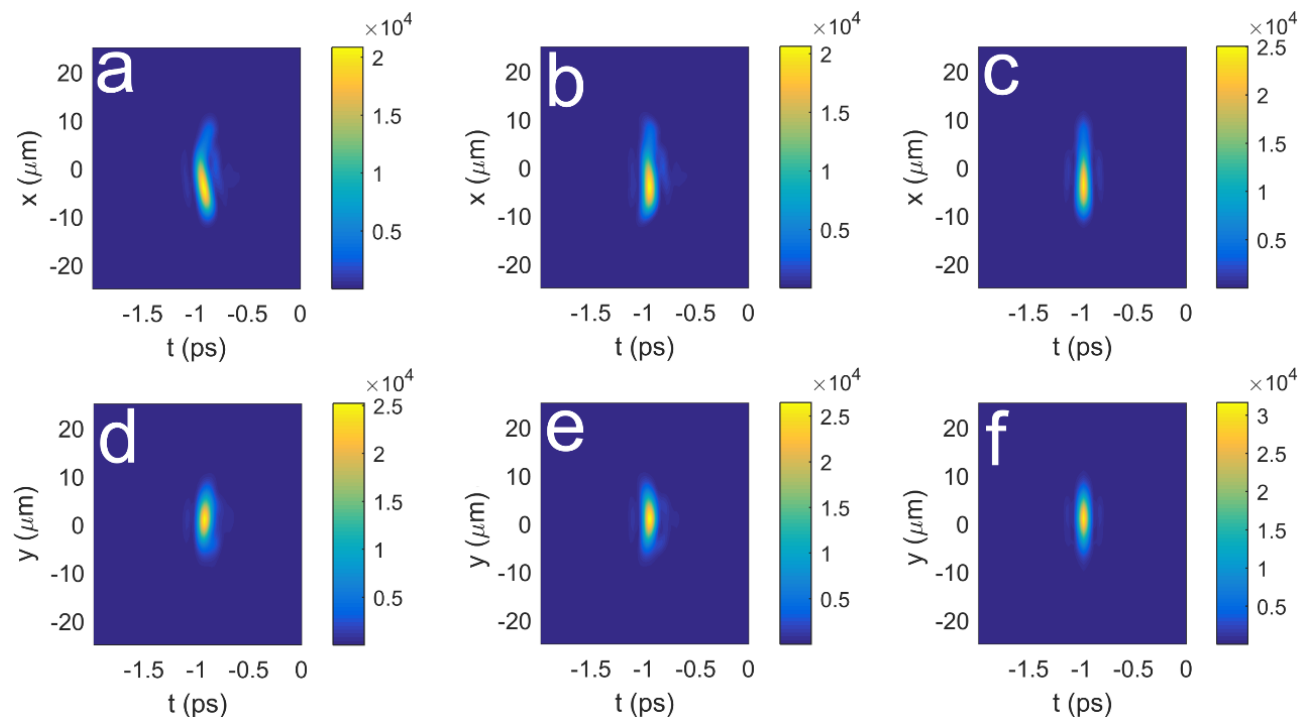
Supplementary Figure 34 shows the typical output pulse spatiotemporal pulse profile obtained in simulations of the low-power multimode mode-locked laser.

Supplementary Figures 35 and **36** show this pulse after quadratic group velocity dispersion compensation, and after spatiotemporal dispersion compensation.

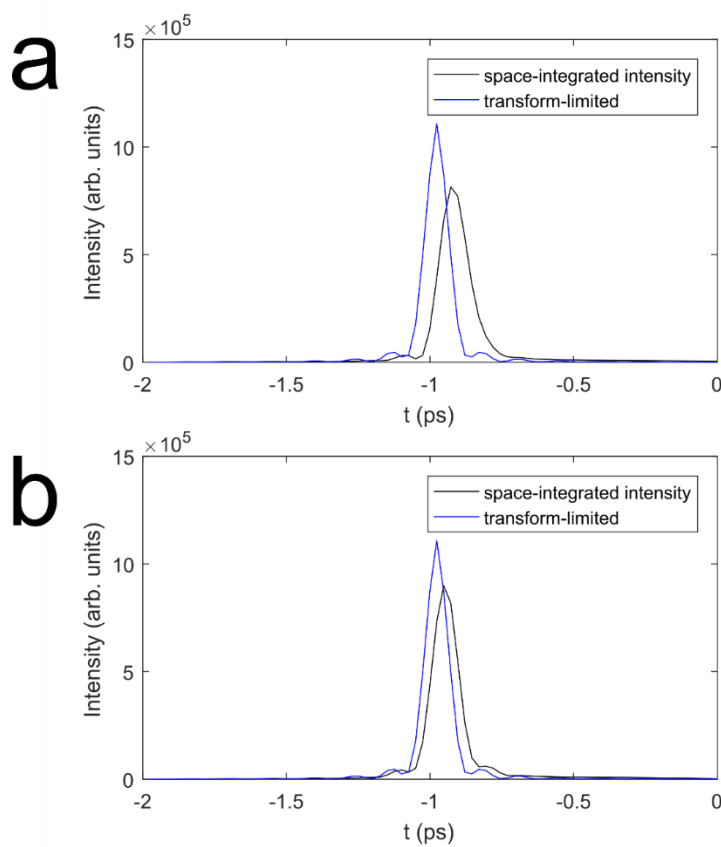
Supplementary Figures 37-39 consider spatiotemporally mode-locked pulses for which conventional dispersion compensation and simple spatiotemporal dispersion compensation are insufficient to reach the transform limit (these very multimode pulses are also shown in **Supplementary Figure 7-8**). These results are similar to those observed experimentally, shown in **Supplementary Figures 39**.



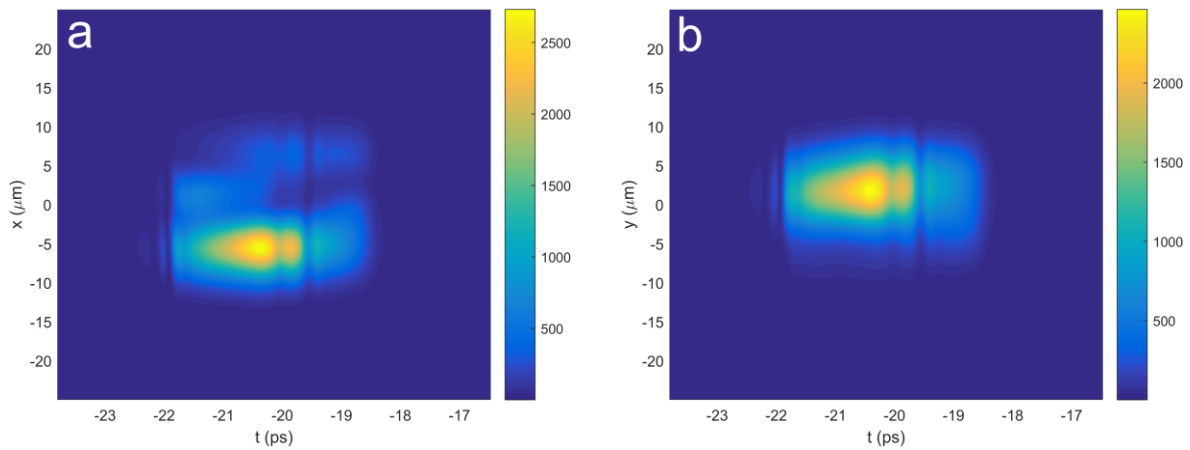
Supplementary Figure 34: Spatiotemporal intensities for the output chirped pulse for numerical simulations of a MM mode-locked laser. The pulses correspond to the numerical simulations shown in **Supplementary Figures 3-6**. **a.** the intensity integrated over the x -dimension, **b.** the intensity integrated over the y -dimension.



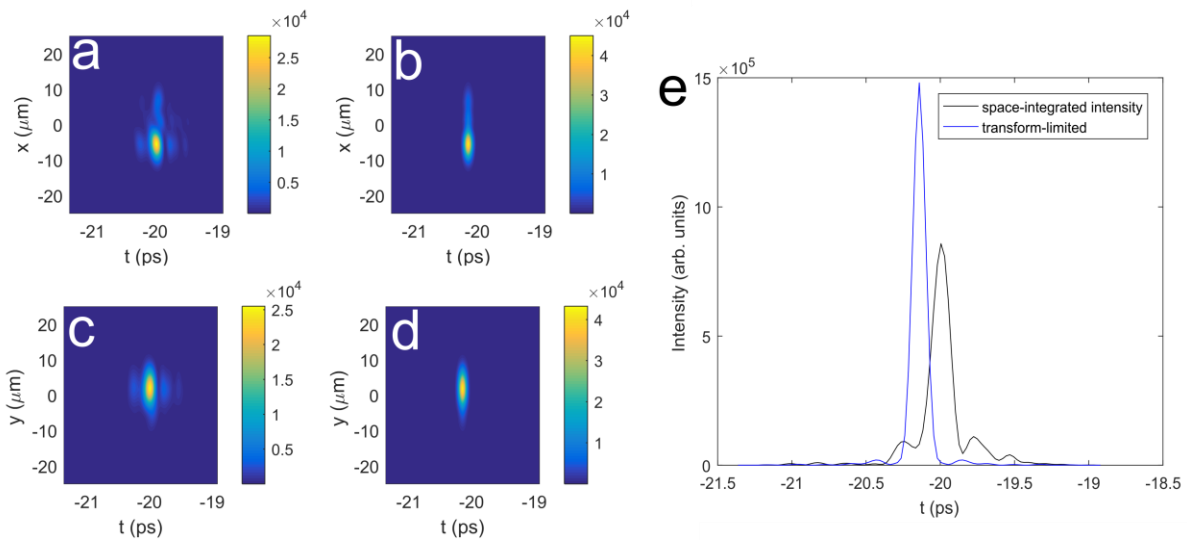
Supplementary Figure 35: Spacetime profiles, integrated over 1 spatial dimension, for different dispersion compensations. **a.** the y -integrated spacetime profile after optimal group velocity dispersion compensation only, **b.** the optimal profile after spatiotemporal dispersion compensation, and **c.** the temporally-transform limited spatiotemporal intensity profile. **d-f** show the same for the x -integrated profile. Quadratic spatiotemporal dispersion means that we apply quadratic spectral phase (i.e., as introduced by an ideal grating compressor) and quadratic spatial group delay (i.e., such as is introduced by a glass lens). Here, the amount of quadratic spatial group delay applied is quite small, and is comparable to the amount introduced by the collimating and imaging lenses used in our experiments.



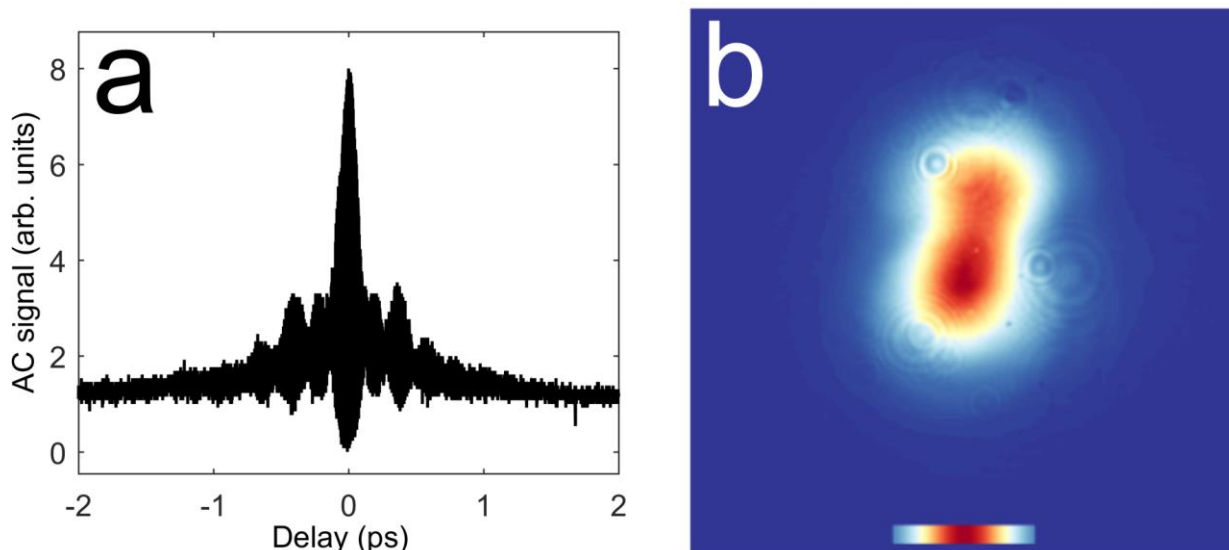
Supplementary Figure 36: Space-integrated temporal intensity profiles for group-velocity and spatiotemporal dispersion compensation. The plots show the intensity profile of the pulse after integrating over both spatial dimensions. The blue curves shows the temporally-transform limited pulse intensity, while the black curves show **a.** the intensity after group velocity dispersion compensation, and **b.** after quadratic spatiotemporal dispersion compensation.



Supplementary Figure 37: Chirped output pulse spatiotemporal profiles, integrated over each space dimension, for a spatiotemporally mode-locked pulse which cannot be efficiently compressed to its transform limit by quadratic spatiotemporal dispersion. See also Supplementary Figures 7-8.



Supplementary Figure 38: Result of quadratic spatiotemporal dispersion compensation, compared to the transform-limited pulse, for the numerical example shown in the previous figure and Supplementary Figures 7-8. a. and c. show the spatiotemporal profiles, integrated over each spatial dimension, after applying the quadratic spatial and spectral phases that produce the maximum peak intensity. b. and d. show the corresponding transform-limited spatiotemporal profiles. e. shows the temporal pulse intensity, integrated over both spatial dimensions, for the transform-limited and optimal quadratic spatiotemporal dispersion compensation. For this highly multimode pulse, mode-locking is only marginally stable and the optimally quadratically-compensated pulse has a peak intensity $\sim 50\%$ of the transform-limit, with prominent temporal sidelobes.



Supplementary Figure 39: Experimental measurements of a spatiotemporally mode-locked pulse exhibiting similar features as the previous numerical results. The results were obtained using a similar cavity as the low power one described in the methods. **a.** the interferometric autocorrelation, and **b.** the near-field beam profile (the scale bar shows the Gaussian profile of the fundamental mode of the fiber, which has a 13 μm mode-field diameter). The comparison is not meant to be direct, since many features of the experiment cannot be adequately measured (e.g., the coupling coefficients into and out of the multimode GRIN fiber). However, the measurements suggest a similar spatiotemporal structure as depicted in **Supplementary Figures 37-38**, suggesting that strongly spatiotemporally dispersed, multimode pulses are observed experimentally.

SUPPLEMENTARY REFERENCES

1. L.G. Wright, W.H. Renninger, D.N. Christodoulides & F.W. Wise. Spatiotemporal dynamics of multimode optical solitons. *Opt. Express* **23**, 3492–506 (2015).
2. P. Horak & F. Poletti, in *Recent Prog. Opt. Fiber Res.* (Yasin, M.) 3–24 (2012)
3. S.-S. Yu, C.-H. Chien, Y. Lai & J. Wang, Spatio-temporal solitary pulses in graded-index materials with Kerr nonlinearity, *Opt. Commun.* **119**, 167–170 (1995).
4. S. Raghavan & G. P. Agrawal, Spatiotemporal solitons in inhomogeneous nonlinear media, *Opt. Commun.* **180**, 377–382 (2000).
5. W. H. Renninger & F. W. Wise, Optical solitons in graded-index multimode fibres, *Nat. Commun.* **4**, 1719 (2013).
6. A. Chong, W.H. Renninger & F.W. Wise, Properties of normal-dispersion femtosecond fiber lasers, *J. Opt. Soc. Am. B* **25**, 140-148 (2008)
7. S. Akturk, Y. Gu, P. Bownan & R. Trebino, Spatio-temporal couplings in ultrashort laser pulses, *J. Opt.* **12**, 093001 (2010).
8. Krupa, K. *et al.* Spatial beam self-cleaning in multimode fibre. *Nat. Photon.* (2017).
9. L.G. Wright, Z. Liu, D.A. Nolan, M.-J. Li, D.N. Christodoulides & F.W. Wise. Self-organized instability in graded-index multimode fibres. *Nat. Photon.* **10** (12), 771-776 (2016).
10. Lopez-Galmiche, G., *et al.* Visible supercontinuum generation in a graded index multimode fiber pumped at 1064 nm. *Opt. Lett.* **41** (11), 2553-2556 (2016).

11. Liu, Z., Wright, L. G., Christodoulides, D. N., & Wise, F. W. (2016). Kerr self-cleaning of femtosecond-pulsed beams in graded-index multimode fiber. *Optics Letters*, *41*(16), 3675-3678.
12. Guenard, R. *et al.* 2017. Kerr self-cleaning of pulsed beam in an ytterbium doped multimode fiber. *Opt. Express* **25** (5), 4783-4792 (2017).